Title: Two-billion-year-old evaporites capture Earth's great oxidation

Authors: C.L. Blättler[1]*, M.W. Claire[2,3,4], A.R. Prave[2], K. Kirsimäe[5], J.A. Higgins[1], P.V. Medvedev[6], A.E. Romashkin[6], D.V. Rychanchik[6], A.L. Zerkle[2,3], K. Paiste[7], T. Kreitsmann[5], I.L. Millar[8], J.A. Hayles[9], H. Bao[10], A.V. Turchyn[11], M.R. Warke[2], A. Lepland[12,7,5,13]

Affiliations:

[1]Department of Geosciences, Princeton University, Princeton, NJ 08544, USA.

[2]School of Earth and Environmental Sciences, University of St Andrews, St Andrews KY16 9AL, Scotland/UK.

[3]Centre for Exoplanet Science, University of St Andrews, St Andrews KY16 9AL, Scotland/UK.

[4]Blue Marble Space Institute of Science, 1001 4th Ave., Suite 3201 Seattle, WA 98154, USA.

[5]University of Tartu, Department of Geology, 50411 Tartu, Estonia.

[6]Institute of Geology, Karelian Science Centre, Pushkinskaya 11, 185610 Petrozavodsk, Russia.

[7]Centre for Arctic Gas Hydrate, Environment and Climate, Department of Geosciences, UiT The Arctic University of Norway, 9037 Tromsø, Norway.

[8]NERC Isotope Geosciences Laboratory, British Geological Survey, Keyworth, Nottingham NG12 5GG, UK.

[9]Department of Earth Science, Rice University, 6100 Main St., Houston, TX 77005, USA.

[10]Department of Geology and Geophysics, E235 Howe-Russell Geoscience Complex, Louisiana State University, Baton Rouge, Louisiana 70803, USA.

[11]Department of Earth Sciences, University of Cambridge, Downing Street, Cambridge CB2 3EQ, UK.

[12]Geological Survey of Norway, 7491 Trondheim, Norway.

[13]Tallinn University of Technology, Institute of Geology, 19086 Tallinn, Estonia.

*Correspondence to: blattler@princeton.edu.

Abstract:

Major changes in atmospheric and ocean chemistry occurred in the Paleoproterozoic Era (2.5–1.6 billion years ago). Increasing oxidation dramatically changed Earth's surface, but few quantitative constraints exist on this important transition. This study describes the sedimentology, mineralogy, and geochemistry of a two-billion-year-old and ~800 meter-thick evaporite succession from the Onega Basin in Russian Karelia. The deposit consists of a basal unit dominated by halite (~100 meters) followed by anhydrite-magnesite (~500 meters) and dolomite-magnesite (~200 meters) dominated units. The evaporite minerals provide a robust constraint that marine sulfate concentrations were at least 10 mmol/kg, representing an oxidant reservoir equivalent to over 20% of the modern ocean-atmosphere oxidizing capacity. These results show that substantial amounts of surface oxidant accumulated during this critical transition in Earth's oxygenation.

One Sentence Summary:

A well preserved, extensive evaporite deposit reveals that a large oxidant reservoir in the form of marine sulfate accumulated two billion years ago.

Main Text:

The geological record preserves evidence of Earth's dynamic surface oxygenation (reviews by *1, 2*), but quantifying this history remains a challenge. The presence/absence of redbeds, banded iron formations, and detrital grains of pyrite and uraninite (*1, 3*) qualitatively indicate increasing oxidation during the Paleoproterozoic, and the disappearance of large-

magnitude mass-independent fractionation (MIF) of sulfur isotopes at 2.4–2.3 Ga (*4, 5*) shows that the atmosphere exceeded a redox threshold of ~1 ppm pO_2 (*6, 7*). However, this limit reflects only a tiny fraction of the potential surface oxidant budget and does not capture subsequent redox changes in the Earth system. Today, marine sulfate ($[SO_4^{2-}{}_{(aq)}]$ = 28 mmol/kg) constitutes one of the largest surface oxidant reservoirs, equivalent to almost twice the modern atmospheric O_2 inventory. Therefore, quantitative bounds on marine sulfate concentrations are essential for constraining the net electron balance and accumulation of oxidants on Earth's surface.

Sedimentary evaporite minerals are one of the best archives of ancient seawater chemistry (e.g. *8, 9*) and specific isotopic signals (e.g. *10, 11*). Unfortunately, most Precambrian evaporite deposits consist of pseudomorphic replacements (*12*), and until recently, the oldest known preserved evaporitic halite and bedded sulfates dated from ~830 Ma (*13, 14*) and ~1.2 Ga (*15*), respectively. This study presents analyses from a remarkably preserved ~2.0 Ga marine evaporite succession bearing carbonates, sulfates, halites, and bittern salts. This succession was discovered during the 2007–2009 drilling of the Onega Parametric Hole (OPH), which intersected 2.9 km of Paleoproterozoic sedimentary and volcanic rocks and 600 m of Archean gneiss in the Onega Basin, Karelia, Russia (*16, 17*). By extending the record of extensive marine evaporites by almost a billion years, core samples from the OPH provide a unique window into surface conditions and redox balance in the aftermath of the initial rise of oxygen on Earth.

The interval of the OPH studied here lies between 2940 and 2115 m depth and corresponds to the ~2.0 Ga Tulomozero Formation (age discussed in supplementary materials). In other cores and outcrop exposures, this formation contains abundant pseudomorphic replacements of evaporite minerals (*18, 19*), but original evaporite minerals are only preserved in

the OPH where they define three major units. Unit 1 (2940–2833 m; 40% average core recovery in cored intervals) comprises dark red-pink, recrystallized halite with intraclasts of anhydrite, magnesite, and mudstone **(Fig. 1A,B)** and ~10% various magnesium- and potassium-sulfate salts **(Fig. 2)**. Unit 2 (2833–2330 m; 56% average core recovery in cored intervals) consists of decimeter- to meter-scale interlayered anhydrite, magnesite, and laminated dark-gray to red mudstone **(Fig. 1C)** with minor glauberite, gypsum, and halite in its lower part. Unit 3 (2330–2115 m; 44% average core recovery in cored intervals) is typified by pink-tan, commonly microbially laminated dolostone **(Fig. 1D)**, laminated red-brown-gray mudstone, and variable amounts of magnesite; quartz and dolomite pseudomorphs of calcium-sulfate minerals occur throughout the lower half of this unit, forming laths, nodules, discs, swallow-tail crystals, and chicken-wire fabric **(Fig. S2)**.

Considering the Tulomozero Formation in the OPH and its development across the 18,000 km^2 of the Onega Basin (*18, 19*), the interpreted depositional setting is a restricted marine embayment with sabkha/coastal plain and shallow-marine environments (**Fig. S3**). The OPH succession captures a decreasing degree of evaporation from a state of halite and magnesium-/potassium-sulfate saturation (Unit 1), through calcium-sulfate deposition (Unit 2), and then to more open marine dolostone precipitation (Unit 3). The extent, thickness (>800 m in the OPH core), and mineral sequence of the evaporite succession are comparable to Phanerozoic evaporite basins.

Isotope geochemistry of the OPH evaporites presents an opportunity to investigate Earth's ocean-atmosphere system at ~2.0 Ga (**Fig. 2**). Quadruple sulfur isotope analyses of samples from Units 1 and 2 reveal $\Delta^{33}S$ and $\Delta^{36}S$ values indistinguishable from zero, confirming an oxic atmosphere (*6, 7*) and production of the Tulomozero Formation sulfate well after that

93 atmospheric transition occurred. Triple oxygen isotope measurements of sulfates yield resolvably
94 negative $\Delta^{17}O$ values. Oxygen MIF derived from atmospheric O_3/O_2 photochemistry (*20*) cannot
95 be ruled out, but the small magnitude $\Delta^{17}O$ signals preclude a unique interpretation (see
96 supplementary materials) and a quantification of pO_2 is not possible.

97 The mass-dependent behavior of sulfur and calcium isotopes provides compositional
98 constraints on ancient seawater. Sulfate $\delta^{34}S$ values lie between 5 and 7‰, except for the
99 uppermost sample in Unit 2 (further discussion in supplementary materials). Given the small ^{34}S
100 enrichment during sulfate evaporite formation (*10*), the seawater sulfate $\delta^{34}S$ composition is
101 estimated to have been 4–6‰ during deposition of Units 1 and 2. The homogeneous sulfur
102 isotopic composition across ~400 m of OPH stratigraphy and the composition and sheer volume
103 of evaporite minerals suggest that the OPH evaporites must have derived from seawater and
104 preserve robust, primary isotopic signals. Additionally, the presence of halite and highly soluble
105 bittern salts in Unit 1 argues against interaction with large volumes of fluid and supports the
106 interpretation of primary isotopic ratios for the major mineral-forming elements. Calcium isotope
107 ratios show a clear stratigraphic relationship following mineralogical trends, with the highest
108 $\delta^{44/40}Ca$ values in Unit 1, decreasing values in Unit 2, and even lower values in Unit 3. Three
109 samples in Unit 3 with the lowest $\delta^{44/40}Ca$ values (–1.6 to –1.4‰ relative to modern seawater)
110 also exhibit relatively high strontium content, with one sample containing minor relict aragonite;
111 these observations indicate that the bulk sediment likely contained primary aragonite which has
112 now largely been converted to other carbonate minerals (see supplementary materials).
113 Excluding those samples associated with aragonite, where mineralogy rather than evaporitic
114 processes is the first-order control on calcium isotope ratios, the increase in $\delta^{44/40}Ca$ values in the
115 more highly evaporated facies is consistent with evaporite precipitation driving isotopic

distillation of calcium, the magnitude of which is sensitive to the initial composition of seawater (*21*).

An estimate for seawater sulfate concentrations at ~2.0 Ga can be derived from the observed sequence, mineralogy, and calcium isotope ratios of the OPH evaporites **(Fig. 3)**. Constraints were assessed by comparison to batch evaporation simulations with varying initial ion concentrations. The relative concentrations of calcium and sulfate are the principal controls governing the precipitation sequence that is expressed in the OPH, as in modern evaporites, of carbonates (Unit 3), followed by calcium sulfates (Unit 2), halite, and eventually magnesium sulfates (Unit 1). As such, the OPH preserves a reversed evaporite sequence where the degree of evaporation decreases stratigraphically upwards, progressing from the most evolved brine at the base of the Tulomozero Formation towards more open marine conditions. During a forward evaporite sequence, calcium precipitates as sulfate minerals and minor carbonate with an isotopic fractionation, such that calcium in the remaining brine becomes enriched in the heavier isotopes through Rayleigh distillation. If sufficient sulfate is present to remove a large fraction of the original calcium content of seawater, later calcium-bearing phases can record large $\delta^{44/40}$Ca enrichments (*21*). The ~1‰ $\delta^{44/40}$Ca range captured in the OPH between shallow-marine carbonates in Unit 3 and halite-hosted anhydrite in Unit 1 therefore places a lower limit on sulfate concentrations. Together with mineralogical constraints, and assuming modern concentrations of other major ions and a conservative interpretation of $\delta^{44/40}$Ca values (but see supplementary materials for further discussion), the minimum sulfate concentration consistent with these observations is ~10 mmol/kg (**Fig. 3**).

The OPH core provides quantitative evidence that marine sulfate concentrations at ~2.0 Ga were at least a third those of modern seawater. This constraint validates assertions that a large

Paleoproterozoic sulfate reservoir existed (*18, 22*) and increases fourfold the previous lower bound of 2.5 mmol/kg sulfate, derived from observing that gypsum evaporites precipitated before halite (*22, 23*). Although the ancient ocean volume is unknown, 10 mmol/kg sulfate in a modern-sized ocean represents an oxidant reservoir equivalent to 23% of the present ocean-atmosphere oxidizing capacity (or 62% of the present atmospheric O_2 inventory). The growth of such a reservoir from < 200 μmol/kg sulfate in the Neoarchean (*24*) would account for a redox imbalance of at least 8–24×10^{10} mol/yr in equivalent moles of O_2 produced or organic carbon buried over 100–300 Myr. Compared to estimates of modern organic carbon burial (5×10^{12} mol/yr (*25*)), the accumulation of such a sizable fluid oxidant reservoir within the given time constraints can be explained by either a large and rapid decline in reductant sinks (i.e. sulfide) or a prolonged 2–5% imbalance over 10^8-year timescales. In either case, the observations suggest that a sustained increase in net O_2 production occurred in the Paleoproterozoic.

The geologically rapid growth of a massive sulfate reservoir, with or without a commensurate increase in atmospheric O_2, also has implications for feedbacks between the global biogeochemical cycles of O_2 and CO_2 and Earth's climate. In particular, the oxidation of large amounts of reduced sulfur requires additional sources of carbon to offset the inferred organic carbon burial (the initial source of oxygen) and prevent catastrophic cooling (*26*). Models for Earth's oxidation must balance these considerations as well as the new evidence for a substantial oxidant reservoir in the form of marine sulfate. Finally, although sulfate likely represented the largest oxidant reservoir during deposition of the Tulomozero Formation, its concentration subsequently decreased such that evaporites at ~1.9 Ga no longer precipitated gypsum before halite (*12, 27*) and a fundamental change in the sedimentary sulfur isotopic composition occurred (*28*). The apparent transient accumulation of surface oxidants is not yet

well understood (*2, 29*) but implies a protracted re-organization of the global redox budget on the timescales of sedimentary recycling of pyrite and organic carbon (i.e. hundreds of millions of years). Regardless of the mechanisms involved, the observations presented here from the OPH core document a remarkably large oxidant pool at ~2.0 Ga – a pivotal new constraint on the history of Earth's oxidation.

References and Notes:

1. D. E. Canfield, The early history of atmospheric oxygen: Homage to Robert M. Garrels. *Annu. Rev. Earth Planet. Sci.* **33**, 1 (2005).

2. T. W. Lyons, C. T. Reinhard, N. J. Planavsky, The rise of oxygen in Earth's early ocean and atmosphere. *Nature* **506**, 307 (2014).

3. H. Holland, in *Early Life on Earth: Nobel Symposium, 84*. (Columbia University Press, 1994).

4. J. Farquhar, H. Bao, M. Thiemens, Atmospheric influence of Earth's earliest sulfur cycle. *Science* **289**, 756 (2000).

5. G. Luo *et al.*, Rapid oxygenation of Earth's atmosphere 2.33 billion years ago. *Science Advances* **2**, e1600134 (2016).

6. A. A. Pavlov, J. F. Kasting, Mass-independent fractionation of sulfur isotopes in Archean sediments: Strong evidence for an anoxic Archean atmosphere. *Astrobiology* **2**, 27 (2002).

7. K. Zahnle, M. Claire, D. Catling, The loss of mass-independent fractionation in sulfur due to a Palaeoproterozoic collapse of atmospheric methane. *Geobiology* **4**, 271 (2006).

8. T. K. Lowenstein, M. N. Timofeeff, S. T. Brennan, L. A. Hardie, R. V. Demicco, Oscillations in Phanerozoic seawater chemistry: Evidence from fluid inclusions. *Science* **294**, 1086 (2001).

9. J. Horita, H. Zimmermann, H. D. Holland, Chemical evolution of seawater during the Phanerozoic: Implications from the record of marine evaporites. *Geochim. Cosmochim. Acta* **66**, 3733 (2002).

10. G. E. Claypool, W. T. Holser, I. R. Kaplan, H. Sakai, I. Zak, The age curves of sulfur and oxygen isotopes in marine sulfate and their mutual interpretation. *Chem. Geol.* **28**, 199 (1980).

11. H. Bao, J. R. Lyons, C. Zhou, Triple oxygen isotope evidence for elevated CO_2 levels after a Neoproterozoic glaciation. *Nature* **453**, 504 (2008).

12. M. C. Pope, J. P. Grotzinger, Paleoproterozoic Stark Formation, Athapuscow Basin, northwest Canada: Record of cratonic-scale salinity crisis. *J. Sediment. Res.* **73**, 280 (2003).

13. N. Spear *et al.*, Analyses of fluid inclusions in Neoproterozoic marine halite provide oldest measurement of seawater chemistry. *Geology* **42**, 103 (2014).

14. J. F. Lindsay, Upper Proterozoic evaporites in the Amadeus basin, central Australia, and their role in basin tectonics. *Geol. Soc. Am. Bull.* **99**, 852 (1987).

15. L. C. Kah, T. W. Lyons, J. T. Chesley, Geochemistry of a 1.2 Ga carbonate-evaporite succession, northern Baffin and Bylot Islands: Implications for Mesoproterozoic marine evolution. *Precambrian Research* **111**, 203 (2001).

16. A. F. Morozov *et al.*, Rock salt mass in the Paleoproterozoic sequence of the Onega Trough in Karelia (from the Onega Parametric Well data). *Doklady Earth Sciences* **435**, 1483 (2010).

17. V. A. Krupenik, K. Y. Sveshnikova, "Correlation of the Onega Parametric Hole with the reference sections of the Onega Structure" in *The Onega Palaeoproterozoic structure (Geology, tectonics, deep structure and minerogeny).* L. V. Glushanin, N. V. Sharov, V. V. Shchiptsov, Eds. (Institute of Geology, Karelian Research Centre RAS, Petrozavodsk, 2011), pp. 190–195 (in Russian).

18. V. A. Melezhik, A. E. Fallick, D. V. Rychanchik, A. B. Kuznetsov, Palaeoproterozoic evaporites in Fennoscandia: Implications for seawater sulphate, the rise of atmospheric oxygen and local amplification of the $\delta^{13}C$ excursion. *Terra Nova* **17**, 141 (2005).

19. A. T. Brasier *et al.*, Coastal sabkha dolomites and calcitised sulphates preserving the Lomagundi-Jatuli carbon isotope signal. *Precambrian Research* **189**, 193 (2011).

20. X. Cao, H. Bao, Dynamic model constraints on oxygen-17 depletion in atmospheric O_2 after a snowball Earth. *PNAS* **110**, 14546 (2013).

21. C. L. Blättler, J. A. Higgins, Calcium isotopes in evaporites record variations in Phanerozoic seawater SO_4 and Ca. *Geology* **42**, 711 (2014).

22. M. Reuschel *et al.*, Isotopic evidence for a sizeable seawater sulfate reservoir at 2.1 Ga. *Precambrian Research* **192**, 78 (2012).

23. S. Schröder, A. Bekker, N. J. Beukes, H. Strauss, H. S. van Niekerk, Rise in seawater sulphate concentration associated with the Paleoproterozoic positive carbon isotope excursion: Evidence from sulphate evaporites in the ~2.2–2.1 Gyr shallow-marine Lucknow Formation, South Africa. *Terra Nova* **20**, 108 (2008).

24. K. S. Habicht, M. Gade, B. Thamdrup, P. Berg, D. E. Canfield, Calibration of sulfate levels in the Archean ocean. *Science* **298**, 2372 (2002).

25. R. A. Berner, D. E. Canfield, A new model for atmospheric oxygen over Phanerozoic time. *Am. J. Sci.* **289**, 333 (1989).

26. A. Bachan, L. R. Kump, The rise of oxygen and siderite oxidation during the Lomagundi Event. *PNAS* **112**, 6562 (2015).

27. J. P. Grotzinger, J. F. Kasting, New constraints on Precambrian ocean composition. *J. Geol.* **101**, 235 (1993).

28. N. J. Planavsky, A. Bekker, A. Hofmann, J. D. Owens, T. W. Lyons, Sulfur record of rising and falling marine oxygen and sulfate levels during the Lomagundi event. *PNAS* **109**, 18300 (2012).

29. A. Bekker, H. D. Holland, Oxygen overshoot and recovery during the early Paleoproterozoic. *Earth Planet. Sci. Lett.* **317**, 295 (2012).

30. V. A. Krupenik, A. M. Akhmedov, K. Y. Sveshnikova, "Isotopic composition of carbon, oxygen and sulphur in the Ludicovian and Jatulian rocks" in *The Onega Palaeoproterozoic structure (Geology, tectonics, deep structure and minerogeny).* L. V. Glushanin, N. V. Sharov, V. V. Shchiptsov, Eds. (Institute of Geology, Karelian Research Centre RAS, Petrozavodsk, 2011), pp. 250–255 (in Russian).

31. V. A. Melezhik *et al.*, Eds., *The Palaeoproterozoic of Fennoscandia as Context for the Fennoscandian Arctic Russia – Drilling Early Earth Project*, vol. 1 of *Reading the Archive of Earth's Oxygenation* (Springer-Verlag, 2013).

32. O. A. Eusipco, I. V. Neronova, "Geophysical studies of the borehole" in *The Onega Palaeoproterozoic structure (Geology, tectonics, deep structure and minerogeny).* L. V. Glushanin, N. V. Sharov, V. V. Shchiptsov, Eds. (Institute of Geology, Karelian Research Centre RAS, Petrozavodsk, 2011), pp. 237-247 (in Russian).

33. O. A. Eusipco, I. V. Neronova, N. V. Sharov, *Geophysical Study of the Onega Parametric Borehole, Lennex Corporation Report*. (Nobel Press, 2014), pp. 62 (in Russian).

34. P. V. Medvedev, V. V. Makarikhin, A. I. Golubev, D. V. Rychanchik, N. N. Trofimov, "The Jatuli" in *The Onega Palaeoproterozoic structure (Geology, tectonics, deep structure and minerogeny).* L. V. Glushanin, N. V. Sharov, V. V. Shchiptsov, Eds. (Institute of Geology, Karelian Research Centre RAS, Petrozavodsk, 2011), pp. 52–67 (in Russian).

35. Y. A. Karpychev, Variations in the sedimentation in Kara Bogaz Gol Bay related to sea level fluctuations during the Novocaspian time. *Oceanology* **47**, 857 (2007).

36. A. N. Kosarev, A. G. Kostianoy, I. S. Zonn, Kara-Bogaz-Gol Bay: Physical and chemical evolution. *Aquatic Geochemistry* **15**, 223 (2009).

37. L. R. Kump *et al.*, Isotopic evidence for massive oxidation of organic matter following the Great Oxidation Event. *Science* **334**, 1694 (2011).

38. A. V. Stepanova, A. V. Samsonov, A. N. Larionov, The final episode of middle Proterozoic magmatism in the Onega structure: Data on trans-Onega dolerites. *Proceedings of the Karelian Research Centre of the Russian Academy of Sciences: Precambrian Geology* **1**, 3 (1998).

39. G. V. Ovchinnikova *et al.*, Pb-Pb age of Jatulian carbonate rocks: the Tulomozero Formation of southeast Karelia. *Stratigraphy and Geological Correlation* **15**, 359 (2007).

40. I. S. Puchtel *et al.*, Petrology of mafic lavas within the Onega plateau, central Karelia: Evidence for 2.0 Ga plume-related continental crustal growth in the Baltic Shield. *Contrib. Mineral. Petrol.* **130**, 134 (1998).

41. A. P. Martin *et al.*, Multiple Palaeoproterozoic carbon burial episodes and excursions. *Earth Planet. Sci. Lett.* **424**, 226 (2015).

42. J. C. Taylor, Computer programs for standardless quantitative analysis of minerals using the full powder diffraction profile. *Powder Diffraction* **6**, 2 (1991).

43. H. Bao, Purifying barite for oxygen isotope measurement by dissolution and reprecipitation in a chelating solution. *Analytical Chemistry* **78**, 304 (2006).

44. H. Bao, M. H. Thiemens, Generation of O_2 from $BaSO_4$ using a CO_2−laser fluorination system for simultaneous analysis of $\delta^{18}O$ and $\delta^{17}O$. *Analytical Chemistry* **72**, 4029 (2000).

45. H. Bao, X. Cao, J. A. Hayles, Triple oxygen isotopes: fundamental relationships and applications. *Annu. Rev. Earth Planet. Sci. Lett.* **44**, 463 (2016).

46. P. W. Crockford *et al.*, Triple oxygen and multiple sulfur isotope constraints on the evolution of the post-Marinoan sulfur cycle. *Earth Planet. Sci. Lett.* **435**, 74 (2016).

47. D. E. Canfield, R. Raiswell, J. T. Westrich, C. M. Reaves, R. A. Berner, The use of chromium reduction in the analysis of reduced inorganic sulfur in sediments and shales. *Chem. Geol.* **54**, 149 (1986).

48. H. G. Thode, J. Monster, H. B. Dunford, Sulphur isotope geochemistry. *Geochim. Cosmochim. Acta* **25**, 159 (1961).

49. G. Antler, A. V. Turchyn, V. Rennie, B. Herut, O. Sivan, Coupled sulfur and oxygen isotope insight into bacterial sulfate reduction in the natural environment. *Geochim. Cosmochim. Acta* **118**, 98 (2013).

50. C. L. Blättler, N. R. Miller, J. A. Higgins, Mg and Ca isotope signatures of authigenic dolomite in siliceous deep-sea sediments. *Earth Planet. Sci. Lett.* **419**, 32 (2015).

51. E. D. Young, A. Galy, H. Nagahara, Kinetic and equilibrium mass-dependent isotope fractionation laws in nature and their geochemical and cosmochemical significance. *Geochim. Cosmochim. Acta* **66**, 1095 (2002).

52. G. Caro, D. A. Papanastassiou, G. J. Wasserburg, ^{40}K–^{40}Ca isotopic constraints on the oceanic calcium cycle. *Earth Planet. Sci. Lett.* **296**, 124 (2010).

53. A. Heuser, A. Eisenhauer, The calcium isotope composition ($\delta^{44/40}Ca$) of NIST SRM 915b and NIST SRM 1486. *Geostandards and Geoanalytical Research* **32**, 311 (2008).

54. A. D. Jacobson, M. G. Andrews, G. O. Lehn, C. Holmden, Silicate versus carbonate weathering in Iceland: New insights from Ca isotopes. *Earth Planet. Sci. Lett.* **416**, 132 (2015).

55. D. L. Parkhurst, C. A. J. Appelo, "User's guide to PHREEQC (Version 2): A computer program for speciation, batch-reaction, one-dimensional transport, and inverse geochemical calculations." *USGS Water-Resources Investigations Report 99-4259* (1999).

56. S. Das Sharma, D. J. Patil, K. Gopalan, Temperature dependence of oxygen isotope fractionation of CO_2 from magnesite-phosphoric acid reaction. *Geochim. Cosmochim. Acta* **66**, 589 (2002).

57. E. D. Young, A. Galy, The isotope geochemistry and cosmochemistry of magnesium. *Rev. Mineral. Geochem.* **55**, 197 (2004).

58. J. A. Karhu, H. D. Holland, Carbon isotopes and the rise of atmospheric oxygen. *Geology* **24**, 867 (1996).

59. A. B. Kuznetsov *et al.*, Sr isotopic composition of Paleoproterozoic ^{13}C-rich carbonate rocks: The Tulomozero Formation, SE Fennoscandian Shield. *Precambrian Research* **182**, 300 (2010).

60. V. A. Melezhik, A. E. Fallick, P. V. Medvedev, V. V. Makarikhin, Palaeoproterozoic magnesite: Lithological and isotopic evidence for playa/sabkha environments. *Sedimentology* **48**, 379 (2001).

61. J. K. Warren, Evaporites through time: Tectonic, climatic and eustatic controls in marine and nonmarine deposits. *Earth-Science Reviews* **98**, 217 (2010).

62. C. E. Harvie, J. H. Weare, The prediction of mineral solubilities in natural waters: The Na–K–Mg–Ca–Cl–SO_4–H_2O system from zero to high concentration at 25°C. *Geochim. Cosmochim. Acta* **44**, 981 (1980).

63. R. J. Spencer, L. A. Hardie, Control of seawater composition by mixing of river waters and mid-ocean ridge hydrothermal brines. *Fluid-mineral interactions: A tribute to HP Eugster: Geochemical Society Special Publication* **19**, 409 (1990).

64. T. K. Lowenstein, M. N. Timofeeff, V. M. Kovalevych, J. Horita, The major-ion composition of Permian seawater. *Geochim. Cosmochim. Acta* **69**, 1701 (2005).

65. T. K. Lowenstein, Origin of depositional cycles in a Permian "saline giant": The Salado (McNutt zone) evaporites of New Mexico and Texas. *Geol. Soc. Am. Bull.* **100**, 592 (1988).

66. R. Langbein, "The Zechstein sulphates: the state of the art" in *The Zechstein Facies in Europe,* T. M. Peryt, Ed. (Springer-Verlag, 1987), pp. 143-188.

67. V. A. Melezhik, A. E. Fallick, P. V. Medvedev, V. V. Makarikhin, Extreme $^{13}C_{carb}$ enrichment in ca. 2.0 Ga magnesite–stromatolite–dolomite–'red beds' association in a global context: A case for the world-wide signal enhanced by a local environment. *Earth-Science Reviews* **48**, 71 (1999).

68. C. E. Harvie, N. Møller, J. H. Weare, The prediction of mineral solubilities in natural waters: The Na-K-Mg-Ca-H-Cl-SO_4-OH-HCO_3-CO_3-CO_2-H_2O system to high ionic strengths at 25°C. *Geochim. Cosmochim. Acta* **48**, 723 (1984).

69. C. M. Bethke, "The Geochemist's Workbench® Release 7.0 (four volumes)" (Hydrogeology Program, University of Illinois, Urbana, Illinois, 2007).

70. J. Huang, Y. Xiao, Mg-Sr isotopes of low-δ^{26}Mg basalts tracing recycled carbonate species: Implication for the initial melting depth of the carbonated mantle in Eastern China. *International Geology Review* **58**, 1350 (2016).

71. J. Schott, V. Mavromatis, T. Fujii, C. R. Pearce, E. H. Oelkers, The control of carbonate mineral Mg isotope composition by aqueous speciation: Theoretical and experimental modeling. *Chem. Geol.* **445**, 120 (2016).

72. T. M. Hensley, "Calcium isotopic variation in marine evaporites and carbonates: Applications to Late Miocene Mediterranean brine chemistry and Late Cenozoic calcium cycling in the oceans", thesis, University of California, San Diego (2006).

73. N. Gussone *et al.*, Calcium isotope fractionation in calcite and aragonite. *Geochim. Cosmochim. Acta* **69**, 4485 (2005).

74. W. T. Holser, "Mineralogy of evaporites" in *Marine minerals,* R. G. Burns, Ed. (Mineralogical Society of America, 1979), vol. 6, pp. 211–294.

75. C. L. Blättler, G. M. Henderson, H. C. Jenkyns, Explaining the Phanerozoic Ca isotope history of seawater. *Geology* **40**, 843 (2012).

76. J. Horita, T. J. Friedman, B. Lazar, H. D. Holland, The composition of Permian seawater. *Geochim. Cosmochim. Acta* **55**, 417 (1991).

346 77. R. J. Spencer, Sulfate minerals in evaporite deposits. *Rev. Mineral. Geochem.* **40**, 173 (2000).

347 78. I. Halevy, A. Bachan, The geologic history of seawater pH. *Science* **355**, 1069 (2017).

348 79. D. A. Fike, A. S. Bradley, C. V. Rose, Rethinking the ancient sulfur cycle. *Annu. Rev. Earth Planet.*
349 *Sci. Lett.* **43**, 593 (2015).

350

351 **Acknowledgements:**

352 Data presented in this study are available in the Supplementary Materials. Funding sources:
353 Simons Foundation (SCOL 339006 to C.L.B.), European Research Council (ERC Horizon 2020
354 grant 678812 to M.C.), Research Council of Norway (RCN Centres of Excellence funding
355 scheme project 223259 to K.P. and A.L.), Estonian Science Agency (PUT696 to K.K., A.L.,
356 K.P., T.K.). Thanks to T.H. Bui for assistance with sulfur isotope analyses and B.A. Wing for
357 helpful discussions. Core material from the Onega Parametric Hole is maintained by the Institute
358 of Geology, Karelian Science Centre, Petrozavodsk.

359

360 **Fig. 1.** Representative Tulomozero Formation evaporite rocks in the OPH. **A.** Halite cored
361 intervals (box length is 1 m; 2900 m depth); note rounded gray intraclasts consisting of
362 mudstone, anhydrite and magnesite. **B.** Halite with felted anhydrite grains and anhydrite-
363 magnesite intraclasts (2854 m depth). **C.** Magnesite-anhydrite (white) and halite overlain sharply
364 by laminated red-gray mudstone with desiccation cracks; magnesite-anhydrite bed infilling
365 compacted desiccation crack at top of image (2528 m depth). **D.** Laminated fine-grained
366 dolostone (2304 m depth). White bars are 1 cm in length.

367

Fig. 2. Interpretive stratigraphy of the Tulomozero Formation in the OPH and associated mineralogical and geochemical data. Calcium isotope data for samples influenced by former aragonite shown by open symbols with crosses. Additional $\delta^{34}S$ from (*30*); cc–calcite, arag–aragonite, dol–dolomite. Methods described in supplementary materials.

Fig. 3. Constraints on seawater chemistry during deposition of the Tulomozero Formation. Circles show batch evaporation simulations with variable calcium and sulfate concentrations; all other ions as in modern seawater. Small, empty circles indicate failure to precipitate gypsum prior to halite. Color of filled circles indicates fraction of initial calcium (f_{Ca}) removed at halite saturation. Conversion of f_{Ca} to $\delta^{44/40}Ca$ range is based on a Rayleigh distillation model with α = 0.99905 (see supplementary materials). M and S identify composition of modern and estimated Silurian seawater (*8*), respectively. Lines indicate constraints from OPH observations (arrows give directionality), and the blue region shows the range of seawater compositions consistent with these constraints.

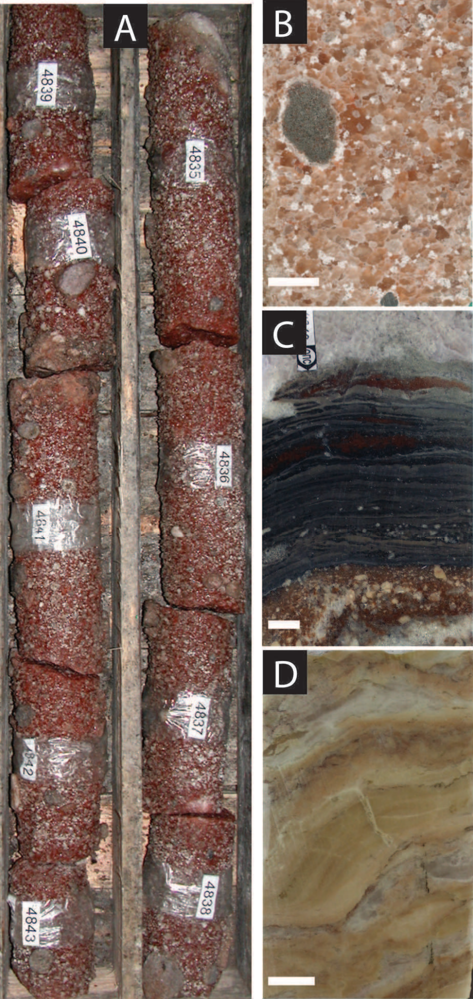
A
B
C
D
4839
4835
4840
4836
4841
4837
842
4843
4838

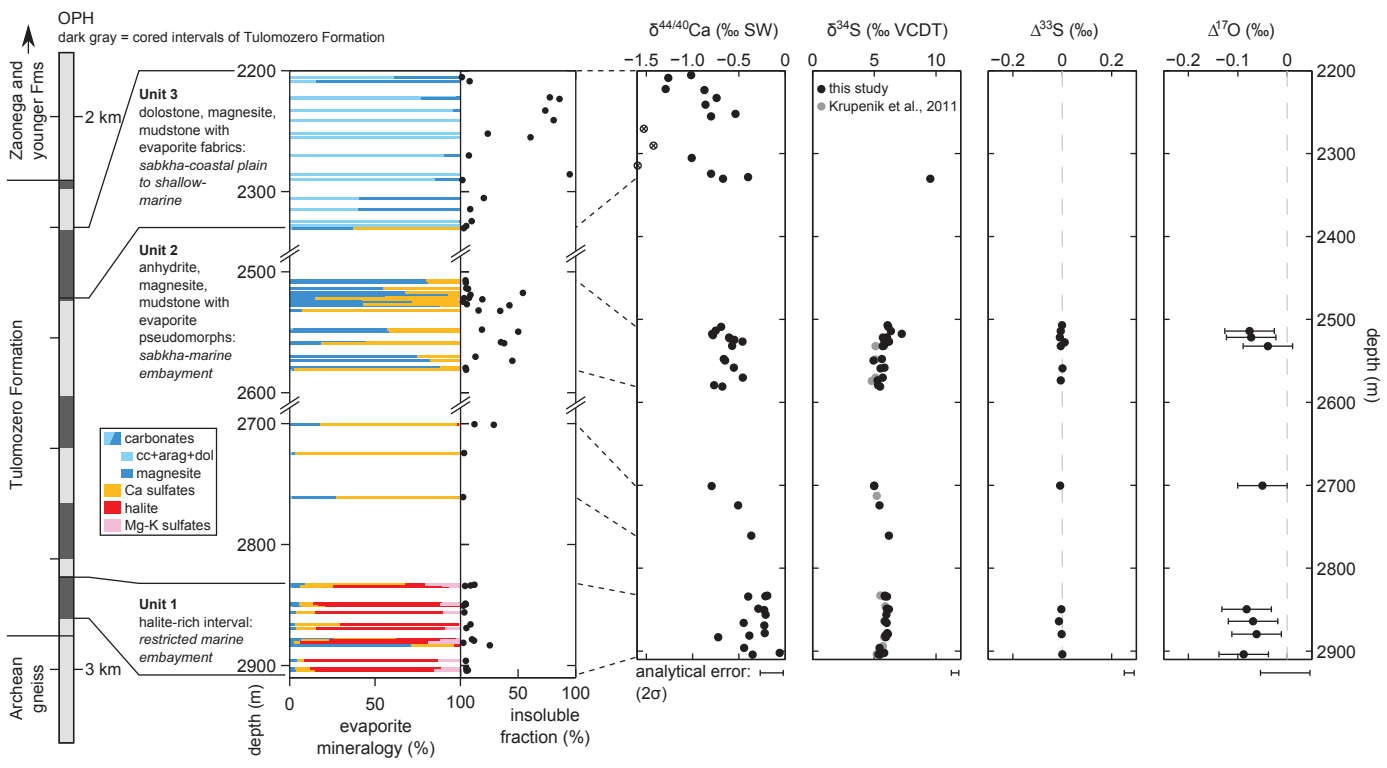
OPH
dark gray = cored intervals of Tulomozero Formation
Zaonega and younger Fms
Tulomozero Formation
Archean gneiss
2 km
3 km
Unit 3
dolostone, magnesite, mudstone with evaporite fabrics: sabkha-coastal plain to shallow-marine
Unit 2
anhydrite, magnesite, mudstone with evaporite pseudomorphs: sabkha-marine embayment
Unit 1
halite-rich interval: restricted marine embayment
carbonates
cc+arag+dol
magnesite
Ca sulfates
halite
Mg-K sulfates
depth (m)
evaporite mineralogy (%)
insoluble fraction (%)
δ44/40Ca (‰ SW)
δ34S (‰ VCDT)
this study
Krupenik et al., 2011
Δ33S (‰)
Δ17O (‰)
analytical error: (2σ)
depth (m)

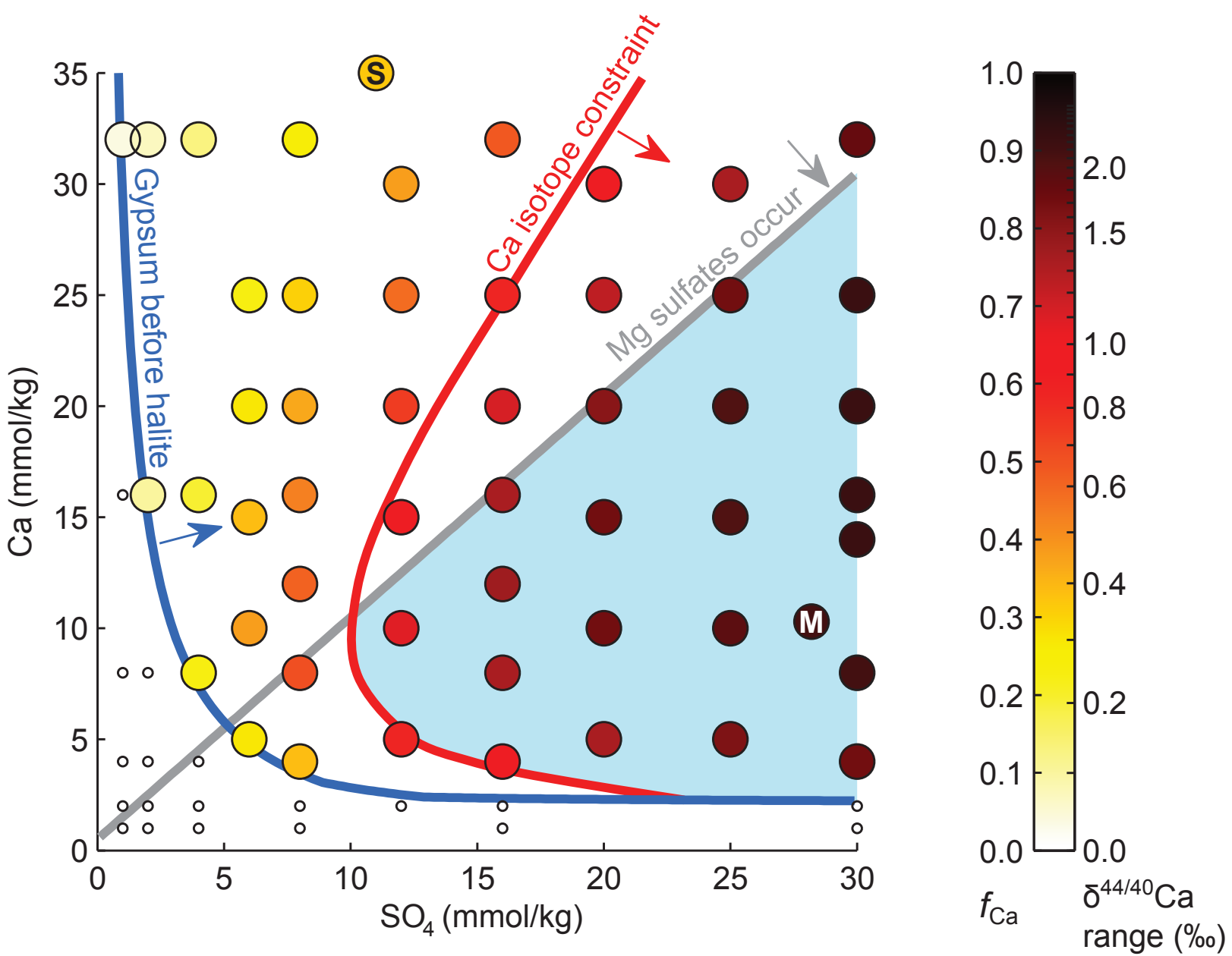
S
M
Gypsum before halite
Ca isotope constraint
Mg sulfates occur
Ca (mmol/kg)
SO4 (mmol/kg)
0
5
10
15
20
25
30
35
fCa
δ44/40Ca range (‰)
0.0
0.1
0.2
0.3
0.4
0.5
0.6
0.7
0.8
0.9
1.0
0.0
0.2
0.4
0.6
0.8
1.0
1.5
2.0

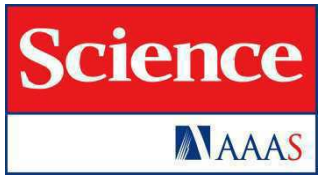

Supplementary Materials for

Two-billion-year-old Evaporites Capture Earth's Great Oxidation

C.L. Blättler, M.W. Claire, A.R. Prave, K. Kirsimäe, J.A. Higgins, P.V. Medvedev, A.E. Romashkin, D.V. Rychanchik, A.L. Zerkle, K. Paiste, T. Kreitsmann, I.L. Millar, J.A. Hayles, H. Bao, A.V. Turchyn, M.R. Warke, A. Lepland

correspondence to: blattler@princeton.edu

This PDF file includes:

Materials and Methods
Supplementary Text
Figs. S1 to S14
Table S1

Other Supplementary Materials for this manuscript include the following:

Data tables S1 to S2

Materials and Methods

Geological context

The Paleoproterozoic sedimentary-volcanic succession in the Onega Basin (Fig. S1) is moderately deformed into open folds cut by high-angle faults and metamorphosed to lower greenschist facies during the 1.85 Ga Svecofennian orogeny (*31*). In the Onega Parametric Hole (OPH), the Tulomozero Formation sits above Archean gneiss and below the conformably overlying Zaonega Formation, composed of siliceous dolomarl-rhythmite and sulfidic fine-grained siliciclastic and carbonaceous rocks. The lower contact with Archean rocks was not recovered, but downhole geophysical data were used to identify contacts in intervals without core recovery and indicate that the halite-dominated unit sits directly on gneiss (*32*). Seismic reflection data (*33*) show that the Tulomozero Formation halite and associated salts form wedge-shaped bodies that thicken west-northwest (from ca. 150 to 400 m over 2 km) and that reflectors have uniformly low-angle dips, indicating that the evaporite units have not undergone significant mass flowage.

Although robust 3-D control for the units dominated by halite and anhydrite-magnesite are lacking (they are only known from the OPH core), the lithofacies associations displayed in the Tulomozero Formation across the Onega Basin indicate that the major evaporite facies was fringed by sabkha-coastal plains and stromatolite reefs (observed in outcrop, e.g. (*34*); Fig. S2). Additional sedimentological features observed in the Tulomozero Formation in the OPH that support a shallow, tidally influenced marine sabkha environment include common desiccation cracks and quartz- and dolomite-pseudomorphed sulfate minerals in the form of laths, swallow-tail-terminating crystals, cauliflower nodules and lenses, and chicken-wire fabric, as well as tidal bundles (cm-scale rhythmic thickening and thinning of layers) and combined-flow ripples with reactivation surfaces and mud drapes. The stromatolite reefs may have acted as barriers restricting exchange of water between the embayment and ocean. Garabogazköl Bay, Turkmenistan offers a partial modern analogue to envisage such a paleogeography (Fig. S3). There, a slender bedrock ridge cut by a narrow inlet separates the Bay from the Caspian Sea; the inlet allows an influx from the Sea with salinities of 1–3% into the Bay where evaporation then raises concentrations to 30–35% in the salt-precipitating areas distal to the inlet (*35, 36*).

Age constraints

The age of the Tulomozero Formation is not precisely constrained. Carbonate carbon isotope ratios in the OPH from this study (see below) and previous work (*30*), as well as other cores in the Onega Basin (*18, 19, 37*), show that the Tulomozero Formation records heavy $\delta^{13}C$ values, in line with the Paleoproterozoic Lomagundi-Jatuli positive carbonate $\delta^{13}C$ excursion. The formation is older than 1956 ± 5 Ma, the age of igneous dykes (*38*) that intrude the conformably overlying Zaonega Formation, but a maximum age for deposition remains debated: a Pb-Pb age of 2090 ± 70 Ma has been obtained from Tulomozero Formation carbonates (*39*), but zircons from a putative lava underlying the Formation yielded U-Pb ages of 1976 ± 9 Ma (*40*) and 1975.3 ± 2.8 Ma (*41*). Thus, until resolved, the most judicious depositional age to consider for the Tulomozero Formation is ca. 2.0 Ga.

X-ray diffractometry

Fifty-nine samples were taken for X-ray diffractometry (XRD); these were pulverized by hand with an agate mortar and pestle, and unoriented preparations were made on low-background sample holders of Si single-crystal wafers with high-index surface orientation. Preparations were measured on a Bruker D8 Advance using a Johannson-type Vario 1 focusing primary monochromator providing pure Cu$K\alpha_1$ radiation to minimize peak overlaps. Scans were recorded with a LynxEye detector in the range $2\theta = 2–70°$, with a step size of 0.012° and counting time of 1 second per step. Mineralogical compositions (Data table S1) were modeled and interpreted using the Rietveld algorithm-based codes Topaz and Siroquant 3.0 (*42*); the relative error of quantification is better than 10% for major phases (>5 wt%) and better than 20% for minor phases (<5 wt%).

Triple oxygen isotope and sulfur isotope analysis

Triple oxygen isotope analyses of sulfate were performed at Louisiana State University. Raw samples were treated with 3 M HCl for the extraction of acid-soluble sulfate (gypsum, anhydrite, carbonate-associated sulfate). To the resulting solution, ~4 mL of $BaCl_2$-saturated 3 M HCl was added, resulting in the quantitative precipitation of $BaSO_4$ which was then washed in distilled and deionized water until the washing solution was pH-neutral. The resulting $BaSO_4$ powders were purified by repeated diethylene-triaminepentaacetic acid (DTPA) dissolution and reprecipitation (*43*). This purification procedure is critical for the removal of nitrate. Purified $BaSO_4$ samples were converted to O_2 by heating with a CO_2-laser under BrF_5. The O_2 from laser fluorination was analyzed for its triple oxygen isotope composition on a Thermo Finnigan MAT 253 (*44*). All reported $\Delta^{17}O$ values are the average of triplicate measurements and were computed using the logarithmic delta-prime notation with $\lambda = 0.52$ to facilitate comparison with published data: $\Delta^{17}O = \delta'^{17}O - 0.52 \cdot \delta'^{18}O$, where $\delta'^{x}O = \ln(\delta^{x}O/1000 + 1) \cdot 1000$. The precision on $\Delta^{17}O$ values is better than ± 0.05‰.

The triple oxygen isotope composition is additionally reported using $\lambda = 0.5305$ (Data table S2). This alternate reference frame (*45*) is considered more appropriate for small magnitude $\Delta^{17}O$ anomalies. The correction is performed using the more accurate $\delta'^{18}O$ from TCEA results (high temperature conversion elemental analyzer): $\Delta^{17}O_{0.5305} = (0.52 \cdot \delta'^{18}O_{TCEA} + \Delta^{17}O_{0.52}) - 0.5305 \cdot \delta'^{18}O_{TCEA}$. Following this correction, the OPH samples average $\Delta^{17}O_{0.5305} = –0.19 \pm 0.03$‰ (1 s.d.). Such small magnitude $\Delta^{17}O$ values can have several origins, including but not restricted to stratospheric photochemical effects involving O_2 and O_3, which are in turn functions of the photosynthetic oxygen flux, oxygen consumption via respiration and weathering, the total atmospheric oxygen reservoir size (pO_2), and its relative size to pCO_2 (*20*). Additional processes such as low-temperature equilibrium fractionation and microbial sulfate cycling are also possible sources of the $\Delta^{17}O$ signal.

Multiple sulfur isotope analyses were conducted on these same purified sulfate samples at McGill University, following an established methodology (*46*). Sulfate samples were purified with a chromium reduction procedure and converted to H_2S gas through reaction with a Thode reduction solution (*47, 48*). The sulfide gas was captured as ZnS, converted to AgS_2, and finally converted to SF_6 gas through reaction with excess

F_2. The resulting SF_6 was purified cryogenically and chromatographically, and its isotopic composition was quantified via gas source mass spectrometry on a Thermo Finnigan MAT 253. Long-term reproducibility (2σ) for $\delta^{34}S$ values is better than ± 0.2‰, and for $\Delta^{33}S$ and $\Delta^{36}S$ values is ± 0.02‰ and ± 0.4‰, respectively. Triple-isotope and Δ-Δ plots (Fig. S4) demonstrate the relationships among the multiple sulfur isotopes.

Additional sulfate $\delta^{34}S$ measurements were performed at the University of Cambridge in the Godwin Laboratory, following previously described methods (*49*). Samples were dissolved in deionized water over 4–5 hours and sulfate was precipitated from the supernatant as barite by adding a saturated barium chloride solution. The barite precipitate was rinsed with deionized water, then dried and combusted at 1030 °C in a Flash Element Analyzer (EA) with the resulting sulfur dioxide (SO_2) analyzed by continuous flow gas source isotope ratio mass spectrometry (Thermo Delta V Plus) and $\delta^{34}S$ values corrected to NBS 127 = 20.3‰. The error for these $\delta^{34}S_{sulfate}$ analyses is 0.3‰ based on replicate analyses of standards.

Calcium isotope analysis

Calcium isotope ratios were measured at Princeton University on fractions of the powdered samples used for XRD. The bulk powders were dissolved in 0.1 M buffered acetic acid–ammonium hydroxide solution (pH of ~4.5) for four hours. The soluble phase was then diluted and introduced into an automated ion chromatograph (Thermo-Dionex ICS-5000$^+$) with a fraction collection system to isolate calcium for isotopic analysis (*50*). The isotope ratios therefore reflect the sum of calcium from all soluble calcium-bearing phases in a given sample, predominantly anhydrite and dolomite with minor gypsum, calcite, and aragonite (Data table S1).

Mass spectrometry was performed on a Thermo Neptune Plus multi-collector inductively coupled plasma mass spectrometer (ICP-MS) with an ESI Apex-IR sample introduction system (*50*). Corrections for isobaric strontium interferences were based on the double-charged ^{87}Sr peak; polyatomic interferences (predominantly argon hydride, carbon dioxide, and nitrous oxide) were avoided with sufficient mass resolution. Sample-standard bracketing was used to calculate $\delta^{44/42}Ca$ values relative to modern seawater. A triple-isotope plot shows the expected mass dependence among ^{44}Ca, ^{43}Ca, and ^{42}Ca (Fig. S5). Reported $\delta^{44/40}Ca$ values are calculated following kinetic fractionation laws (*51*) and assuming no radiogenic ^{40}Ca excess, which is consistent with previous work showing a lack of resolvable ^{40}Ca excess in modern seawater or ancient marine precipitates (*52*); alternatively, these can be considered initial $\delta^{44/40}Ca$ values. External precision on $\delta^{44/40}Ca$ values is ± 0.14‰ (2σ), derived from the long-term reproducibility of the carbonate standard SRM-915b (n=155). The $\delta^{44/40}Ca$ value obtained for SRM-915b is –1.15‰, which is indistinguishable from published values (*53, 54*).

Evaporation simulations

Evaporation simulations were conducted with the PHREEQC program (*55*) by the U.S. Geological Survey (https://wwwbrr.cr.usgs.gov/projects/GWC_coupled/phreeqc/). Simulations were initialized with varying concentrations of carbonate alkalinity, calcium, chloride, potassium, magnesium, sodium, sulfate, and trace strontium and set in equilibrium with $pCO_2 = 10^{-1.5}$ atm (100× pre-industrial, see below for further

explanation) at a temperature of 25 °C with no charge balance imposed (i.e. net positive or negative charges were permitted and remained constant throughout a single simulation). The minerals in Table S1 were permitted to precipitate if the respective saturations were attained. Note that calcite was the only carbonate mineral included; dolomite and magnesite precipitation were suppressed because of known kinetic barriers (see below for discussion of magnesite). The pitzer.dat database provided with PHREEQC was used for thermodynamic speciation and equilibrium calculations during the removal of over 99% of the initial water, and no back-reactions were allowed between fluid and solid phases.

Simulated evaporation of modern seawater yields a mineral assemblage of calcite, celestine, gypsum, glauberite, halite, polyhalite, bloedite, epsomite, kainite, kieserite, carnallite, and bischofite (listed in order of appearance with progressive evaporation). Simulated evaporation of estimated Silurian seawater (*8*) yields a distinctly different assemblage, notably lacking magnesium sulfate minerals, of calcite, gypsum, halite, anhydrite, sylvite, carnallite, bischofite, and $MgCl_2$ tetrahydrate. The constraints in Fig. 3 (main text) were established using simulations to determine the degree of evaporation (= initial water content / final water content) for the initial appearance of gypsum and halite, the presence/absence of select evaporite minerals, and the fraction of calcium removed at the onset of halite precipitation (see below for discussion of interpreting calcium isotopes and sensitivity tests of simulation behavior). The results using PHREEQC differ notably from simple calculations relying on stoichiometric relationships among the major ions because of variable ion activities in concentrated brines.

Supplementary Text

Supporting geochemical data: Methods

Additional geochemical data, including carbonate carbon isotope ratios ($\delta^{13}C$), magnesium isotope ratios ($\delta^{26}Mg$), strontium isotope ratios ($^{87}Sr/^{86}Sr$), and trace element concentrations, provide additional context for the OPH (Data table S2). Carbon isotope ratios in calcium carbonate, dolomite, and magnesite were measured on micro-drilled powdered samples on a Thermo Delta V Advantage continuous flow isotope ratio mass spectrometer at Tartu University. Magnesite and dolomite-magnesite samples were reacted for 96 h at 70 °C to allow for the complete reaction of magnesite (method modified from (*56*)). Dolomite samples with <1 wt% magnesite content, as determined by XRD analysis, were reacted for 2.5 h at 70 °C. Carbon isotope ratios are reported relative to Vienna Pee Dee Belemnite (VPDB) with reproducibility (2σ) better than ± 0.1‰.

Magnesium isotopes and trace elements were measured at Princeton University on the same dissolved fractions used for calcium isotope analysis (see above). For magnesium isotopes, automated ion chromatography (Thermo-Dionex ICS-5000$^+$) was used to isolate magnesium, and isotopic ratios were then obtained by multi-collector ICP-MS (Thermo Neptune Plus) with wet aerosol introduction through a cyclonic spray chamber (*50*). Sample-standard bracketing in low resolution was used to calculate $\delta^{26}Mg$ values relative to the standard DSM3. A triple-isotope plot shows the expected mass dependence among ^{24}Mg, ^{25}Mg, and ^{26}Mg (Fig. S6). External precision on $\delta^{26}Mg$ values is ± 0.09‰ (2σ), derived from the long-term reproducibility of the standard Cambridge-1

(n=76). The δ^{26}Mg value obtained for Cambridge-1 is –2.56‰, which is indistinguishable from published values (*57*).

Trace elements were analyzed on a quadrupole ICP-MS at Princeton University (Thermo iCAP). Samples were diluted so that major cations were no greater than 10 ppm, and scandium was added as an internal standard. External standard calibration curves bracketed the concentrations of each element of interest in the sample solutions, yielding precision of approximately ± 5%. Reported trace element concentrations reflect those of the acetic-acid-soluble component only (sum of carbonate, sulfate, and chloride evaporite minerals), not whole rock concentrations.

Strontium isotopes were analyzed at the NERC Isotope Geosciences Laboratory (British Geological Survey). The powdered samples were first leached in dilute (10%) acetic acid at 50 °C for 30 minutes to remove secondary carbonate phases. Residual material was washed repeatedly in water, then dissolved in distilled 6 M HCl at 50 °C for one hour. The dissolved material was removed after centrifuging, dried down, and converted to nitrate form using 1 mL 16 M HNO_3. Strontium was separated using Sr-SPEC ion exchange resin, loaded onto outgassed single Re-filaments, and analyzed in a Thermo Scientific Triton thermal ionization mass spectrometer operated in multi-dynamic mode with 100 measurement cycles for each sample. Eleven measurements of the strontium standard NBS-987 across the interval of analysis yield $^{87}Sr/^{86}Sr = 0.710256$ (± 0.000007). Five seawater standards analyzed in the same period yield $^{87}Sr/^{86}Sr = 0.709182$ (± 0.000004). The sample $^{87}Sr/^{86}Sr_i$ ratios have been corrected for the age of the Tulomozero Formation (2.0 Ga), and precision (2σ) for all samples is better than ± 0.000011.

Supporting geochemical data: Results

The additional geochemical datasets (Fig. S7 and S8) are generally consistent with the observations and interpretations presented in the main text. The magnesium isotope data are discussed below. Carbonate $\delta^{13}C$ values from dolomite, magnesite, and rarely calcium carbonate range from +8.1 to +13.9‰, except for one sample in Unit 2 showing extreme ^{13}C enrichment at +18.8‰. These values are characteristic of carbonates precipitated during the Lomagundi-Jatuli positive carbonate $\delta^{13}C$ excursion (*58*).

Elevated strontium concentrations are found in three carbonate samples that also have very low $\delta^{44/40}Ca$ values, one of which contains 4% aragonite (detected by XRD). The combined geochemical evidence suggests that aragonite was likely the precursor carbonate mineral for these three samples, and that they were partially/completely converted to calcite, dolomite, and magnesite. The sample with detectable aragonite also contains the highest proportion of calcite (55%) and highest strontium content (690 ppm) of any OPH sample, indicating relatively closed system (sediment-buffered) conditions during early marine neomorphism and recrystallization.

Relatively high strontium is also found in association with the anhydrite-magnesite of Unit 2, and to a lesser degree in Unit 1, where it scales with the abundance of calcium sulfate minerals (Fig. S9). This relationship suggests that where strontium is not associated with aragonite, it may either be substituted into calcium sulfate minerals or exist as strontium sulfate (celestine), a trace phase predicted to co-precipitate with gypsum and anhydrite in evaporation simulations. Manganese is enriched in the

carbonates of Unit 3. High lithium concentrations are present in Unit 1, where it would be expected to substitute into the monovalent salts.

Strontium isotope ratios show a large degree of variability, indicating contamination from radiogenic sources. This is not surprising, given the potential for considerable local ingrowth of ^{87}Sr from ^{87}Rb substituted into potassium-rich salts in the formation. The minimum $^{87}Sr/^{86}Sr_i$ ratio measured in the OPH is 0.7041, which agrees well with the estimated Paleoproterozoic seawater $^{87}Sr/^{86}Sr$ from other samples of the Tulomozero Formation (*59*). There is no obvious stratigraphic trend in the OPH $^{87}Sr/^{86}Sr_i$ ratios. Two outliers with extremely high ratios ($^{87}Sr/^{86}Sr_i$ = 0.7346 and 0.7475) are well outside the range of marine $^{87}Sr/^{86}Sr$ of any age, which requires a local contaminating source of ^{87}Sr. These two outliers also are the most phyllosilicate-rich samples, so it is likely that the leaching/dissolution procedures introduced some silicate-derived radiogenic strontium.

Comment on preservation

The interpretation of geochemical and isotopic signals in the OPH evaporites relies upon their bulk geochemical properties being well preserved. The simple fact that the soluble sulfate, halite, and bittern salts have survived points to limited fluid interaction with the evaporites, otherwise they would easily have been dissolved and/or replaced. Indeed, the dissolution of salts is the inferred cause of breccias in other parts of the Tulomozero Formation and ancient evaporite deposits in general (*19, 60, 61*). Additionally, the majority of geochemical analyses presented in this study are of major stoichiometric constituents of the mineral assemblage. Following mass balance considerations, the major-element geochemistry of rocks is generally strongly buffered against bulk alteration; in the specific case of the OPH, this buffering capacity should be even higher given the thick evaporite deposits and limited post-depositional fluid interaction.

Syn-depositional alteration of primary evaporite sediments, e.g. through brine interaction and authigenic mineral growth, is recognized within the OPH evaporite facies. The presence of sulfate nodules and pseudomorphs in Unit 3 (Fig. S2) may be considered a type of early diagenesis (but note that these features are distinct from the massive bedded sulfates in Unit 2). Most sulfate mineral pseudomorphs in the OPH cause disruption and differential compaction of laminae, indicating that their precipitation was syn-sedimentary to early diagenetic. High glauberite content in a few intervals may be the product of brine-evaporite interaction, as glauberite is known to replace gypsum/anhydrite during progressive evaporation (*62, 63*). During burial and regional deformation, other mineral conversions may also have occurred, including loss/gain of water in hydrated minerals and widespread recrystallization. However, it is difficult to conceive of a process that could have altered the bulk composition of these massive evaporites following burial without dissolving them, leading to the conclusion that mass conservation of the major ions has likely been maintained and the observed isotopic signals are robust.

Comment on magnesite

The abundance of magnesite in the OPH (up to 90 wt%; on average 50 wt% of the soluble fraction in Unit 2) is an unusual feature and warrants further consideration. Petrographic study of thin sections was conducted using a Zeiss EVO MA15 scanning

electron microscope (SEM) equipped with an Oxford Instruments X-MAX energy-dispersive X-ray spectroscopy (EDS) detector. Magnesite is often present as large rhombs, sometimes intergrown with large (mm-long) magnesium silicate crystals (talc, phlogopite) and recrystallized anhydrite, indicating recrystallization of magnesite (Fig. S10A). These large magnesite crystals often show zoning with an outer rim containing elevated iron, indicating changing fluid composition with higher iron (possibly derived from hematite alteration) during magnesite recrystallization. Elsewhere, magnesite shows a different structure and fabric, with beds/lamellae of much smaller magnesite crystals and finely disseminated hematite and silicates including quartz, talc, and phlogopite (Fig. S10D). This fabric and the co-occurrence with hematite suggests that magnesite may have been an early, syn-depositional phase in the OPH.

Evaporitic magnesite is known from Phanerozoic salt formations, including the Wellington Formation (*64*), Salado Formation (*65*), and Zechstein deposits (*66*) of the Permian. In these settings, magnesite has been interpreted as an early diagenetic replacement of precursor carbonate minerals from interaction with brines. Co-precipitation with anhydrite has also been noted (*66*). Similar processes may have been promoted in the OPH, where magnesite is the principal carbonate mineral present in Units 1 and 2, by a combination of high Mg/Ca ratios and pCO_2 in the Paleoproterozoic. Magnesite beds in other Tulomozero Formation cores have similarly been interpreted as early diagenetic products (*60, 67*). A late replacement origin is improbable based on mass balance considerations, since forming massive magnesite requires large volumes of seawater or brine, and the existence of highly soluble evaporite minerals places limits on the volume of fluid that could have interacted with the OPH. Calcium carbonates are also notably absent in the stoichiometric amounts required for closed-system decomposition of dolomite, which also supports an early origin for the magnesite. These observations strengthen the interpretation of calcium isotopes in the OPH by discounting late-stage (post-burial) fluid flow and calcium release from precursor calcium carbonate minerals.

Although the PHREEQC evaporation simulations described above exclude magnesite precipitation, additional evaporation simulations using the Harvie-Møller-Weare activity model in The Geochemist's Workbench 7 (*68, 69*) support the precipitation of magnesite as an evaporitic mineral phase. Equilibrium precipitation of magnesite theoretically occurs under a range of conditions and is sensitive to pCO_2 and relative concentrations of calcium, magnesium, and sulfate (kinetic factors not modeled, despite their likely importance). At pre-industrial pCO_2 ($10^{-3.5}$ atm), batch evaporation of modern seawater yields a mineral precipitation sequence of calcite, gypsum, magnesite, and halite (followed by additional minerals); at 100× pre-industrial pCO_2 ($10^{-1.5}$ atm), simulations yield a sequence of magnesite, gypsum, then halite. As expected, higher seawater Mg/Ca ratios also promote magnesite precipitation in these simulations.

Magnesium isotope ratios in the OPH are also consistent with a syn-depositional or early diagenetic origin for magnesite. Almost all of the magnesium in the soluble fraction comes from magnesite, and Unit 1 has slightly higher $\delta^{26}Mg$ values (by ~0.3‰) than Units 2 or 3 (Fig. S7). If magnesite was a late replacement or hydrothermal phase, homogeneous $\delta^{26}Mg$ values might be expected throughout the core. Although little is known about magnesium isotope behavior in low-temperature evaporitic magnesite, the mineral is generally fractionated towards more negative $\delta^{26}Mg$ values (*70, 71*). It is therefore possible that evaporitic distillation of magnesium isotopes may occur during

magnesite formation, analogous to the behavior of calcium isotopes in evaporitic calcium sulfates. The higher δ^{26}Mg values in Unit 1 might then reflect the removal of lighter magnesium isotopes in earlier evaporite phases and the isotopic enrichment of magnesium in later precipitates. The current lack of knowledge about magnesium isotopes in this type of environment prevents further interpretation of the δ^{26}Mg signal in the OPH.

Interpreting calcium isotopes

The isotopic behavior of calcium in the OPH is interpreted based on comparison to theory, laboratory experiments, and Phanerozoic evaporite sequences (*21*). Theoretically, a batch evaporation system that precipitates calcium carbonate and calcium sulfate minerals will induce Rayleigh distillation in calcium isotopes, with the ratio of ^{44}Ca to ^{40}Ca in the fluid following the relationship ${}^{44/40}R_{\text{fluid}} = {}^{44/40}R_i\,(1 - f_{\text{Ca}})^{\alpha-1}$, where ${}^{44/40}R_i$ is the initial ratio of the fluid, f_{Ca} is the fraction of calcium removed in evaporite minerals, and α is the fractionation factor, equal to ${}^{44/40}R_{\text{precipitate}}/{}^{44/40}R_{\text{fluid}}$. The fractionation factor for evaporitic gypsum precipitation is 0.99905 (*21, 72*), and because gypsum dominates the removal of calcium in evaporites and has an overlapping fractionation factor with that for calcite (approximately 0.9987 to 0.9992 (*73*)), a constant $\alpha = 0.99905$ is assumed for the entire evaporation sequence. The isotopic composition of the minerals precipitated at a given point in time (or a given f_{Ca}) is equal to $\alpha \cdot {}^{44/40}R_{\text{fluid}}$. The isotopic evolution of calcium-bearing minerals will be expressed stratigraphically and can be measured and reported using standard delta notation, $\delta^{44/40}\text{Ca} = ({}^{44/40}R_{\text{sample}}/{}^{44/40}R_{\text{standard}} - 1) \cdot 1000$, where the reference standard is modern seawater.

The range in $\delta^{44/40}$Ca values expressed between the onset of evaporite deposition (the transition from non-restricted to restricted conditions) and halite precipitation can be converted to f_{Ca} (see the dual axes for the color scale in Fig. 3 and Fig. S13). The value of f_{Ca} removed prior to halite saturation then places constraints on the initial fluid composition (see below). The assumptions required to derive these constraints are discussed in this section. In general, the most conservative assumptions have been made to define the largest possible solution space for seawater chemistry; relaxing these assumptions yields only narrower compositional constraints.

Practically, capturing the full theoretical $\delta^{44/40}$Ca range predicted for an evaporite sequence is unlikely. The gypsum or anhydrite deposited just adjacent to halite may not be sampled, and analytical uncertainties of ± 0.14‰ may also truncate (or possibly expand) estimates of the true $\delta^{44/40}$Ca range. Additionally, a batch evaporation model may not be appropriate for evaporite basins, which are typically enriched in the less soluble evaporite minerals relative to the proportions expected from fully evaporating seawater (*74*). This observation invokes an alternative model with a near steady-state hydrological balance between inflow of seawater, evaporation, and outflow of concentrated brines. The isotopic composition of evaporites in a steady-state system would yield lower values than for the Rayleigh model described above because of mixing between seawater and isotopically enriched brines. Collectively, these effects tend to bias the observations towards a smaller $\delta^{44/40}$Ca range than predicted from batch evaporation theory. Indeed, Phanerozoic evaporite sequences for which the composition of seawater can be reconstructed from halite fluid inclusions (*8, 9*) express $\delta^{44/40}$Ca ranges 64–100% of the magnitude predicted by theory (*21*). A similar bias towards a

smaller $\delta^{44/40}$Ca range in the OPH would correspond to an underestimate for f_{Ca} and therefore an expanded solution space for seawater chemistry.

The minimum and maximum $\delta^{44/40}$Ca values that define the observed calcium isotope range are also potential sources of uncertainty. The minimum $\delta^{44/40}$Ca value, normally present in carbonate minerals, can be biased towards lower values if aragonite is present (*73, 75*). For this reason, the three samples where strontium and XRD results suggest the influence of aragonite have been excluded from defining the evaporite-driven $\delta^{44/40}$Ca range. Among the remaining carbonate samples in Unit 3, the next lowest $\delta^{44/40}$Ca values span from –1.3 to –1.0‰. The scatter in calcium isotope ratios within Unit 3 may be associated with the precipitation of sulfate nodules from shallow brines as well as early marine carbonate diagenesis, noting that the heaviest values are found in dolomites. The intermediate values of –0.8 to –0.4‰ recorded in Unit 2 are consistent with an increased degree of evaporation and partial isotopic distillation by calcium sulfates relative to open marine conditions. In Unit 1, the most highly evaporated part of the OPH, the $\delta^{44/40}$Ca value of one sample reaches –0.06‰, while several other samples record values of –0.2‰. The observed range could therefore be taken to be 0.8‰ on the low end or 1.24‰ on the high end, corresponding to f_{Ca} between 0.57 and 0.73. Preferring to underestimate rather than overestimate the observed calcium isotope effect, $f_{Ca} = 0.6$ is chosen for the interpreted $\delta^{44/40}$Ca range in the OPH.

The estimate of $f_{Ca} = 0.6$ is further interpreted to represent the fraction of calcium removed at degrees of evaporation below halite saturation, despite the inclusion of samples from Unit 1 that contain halite. The simplest way to ensure this condition would be to define the maximum $\delta^{44/40}$Ca values by sampling the boundary between Units 1 and 2, where a clear transition from halite saturation to under-saturation occurs. Unfortunately, no samples from that interval could be obtained as a result of limited core recovery. However, the halite-rich samples in Unit 1 are still expected to record the distillation of calcium isotopes at a lower degree of evaporation. Samples from Unit 1 host on average 10–15% anhydrite disseminated within halite and in clasts (broken, rounded anhydrite-magnesite beds), which is much more than the 0.1–1% anhydrite that co-precipitates with halite once halite saturation has been attained. High concentrations of sodium and chloride effectively dilute calcium sulfates to the level of a trace constituent among abundant halite. Therefore, the anhydrite-magnesite clasts sampled in Unit 1 likely reflect evaporite cycles where less concentrated fluids were introduced into the basin. These fluids will express calcium isotope distillation at a lower degree of evaporation as halite saturation is re-approached. After halite saturation is reached, the precipitation of additional calcium-bearing minerals which may record further isotopic enrichments is a negligible component of the total calcium isolated from these samples and therefore should not factor into interpretations of the measured $\delta^{44/40}$Ca values.

Behavior and sensitivity of evaporation simulations

The mineralogical boundaries defined in Fig. 3 (main text) for the occurrence of magnesium sulfates (gray diagonal line) and the appearance of gypsum before halite (blue hyperbolic curve) are also defined conservatively. The boundary where magnesium sulfates first occur is usually identified in PHREEQC simulations by the appearance of kieserite ($MgSO_4 \cdot H_2O$) and exists where calcium and sulfate concentrations are approximately equal. More abundant and diverse magnesium sulfates, e.g. epsomite and

bloedite, occur with higher relative sulfate concentrations. The abundance of magnesium sulfate salts in the OPH, on average 10% in Unit 1, suggests that Paleoproterozoic seawater was not at the limit where magnesium sulfates just barely occur, but had considerably higher sulfate than calcium (towards the lower right in Fig. S11). Note that the position of this mineralogical boundary is largely insensitive to the concentrations of other major ions, including magnesium, as it depends primarily on the existence of excess sulfate following gypsum/anhydrite precipitation (*76, 77*).

The near absence of sylvite in the OPH adds another possible constraint on seawater chemistry, albeit with great uncertainty. Trace sylvite was detected by XRD in a handful of samples, but not as a major mineral component. While this observation may be an artifact of mineral alteration during burial and diagenesis (potassium and chloride may have combined with other ions to form composite salts such as leonite, langbeinite, or kainite), if the lack of sylvite was indeed a primary feature of the OPH mineral assemblage, ancient seawater would be constrained to the lower right of the red dashed line in Fig. S11. The position of this line is sensitive to magnesium and potassium concentrations, which are highly uncertain. As a result, the absence of sylvite should be considered suggestive at best (although the implications for seawater chemistry are consistent with those from the existence of abundant magnesium sulfates, as discussed above).

The appearance of gypsum before halite is sensitive not only to the concentrations of calcium and sulfate, but also to those of sodium, chloride, and alkalinity (Fig. S12). The limit for this behavior has often been defined as >2.5 mM sulfate (*22, 23*), which does not account for these additional dependencies. For example, if calcium concentrations were higher than today, as predicted for intervals of higher pCO_2 and lower $[CO_3^{2-}]$, sulfate could fall below the stated limit and still result in gypsum precipitation prior to halite. In the case of the Tulomozero Formation, the constraint from magnesium sulfates in the OPH largely supersedes the lower limit for sulfate defined by this behavior.

The effect of alkalinity on the appearance of gypsum before halite (Fig. S12, left) stems from the potential for carbonate minerals to deplete calcium that would otherwise be available for gypsum precipitation. In highly alkaline waters, gypsum saturation is delayed to a higher degree of evaporation and may eventually fail to appear in the evaporite assemblage (*77*). Simulations were run in equilibrium with an estimate for Paleoproterozoic pCO_2 at the high end of suggested values (*78*) in order to lower pH and minimize this effect, thus yielding a larger range of calcium and sulfate concentrations that could satisfy the observed OPH mineral sequence. The dependence on sodium and chloride (Fig. S12, right) is explained simply by the saturation of halite occurring at a lower (higher) degree of evaporation and requiring an increase (decrease) in the ion activity product $(Ca)\cdot(SO_4)$ for gypsum to reach saturation before halite. The lighter and darker blue curves represent an increase and decrease, respectively, of both sodium and chloride by approximately 30%, corresponding to an initial ion activity product $(Na)\cdot(Cl)$ of 164% and 51% of that for modern seawater.

The appearance of gypsum before halite is once again a very conservative boundary for defining seawater chemistry for the OPH, considering the thick (~500 m) interval of sulfate-rich evaporites in Unit 2, lying between the halites of Unit 1 and the carbonates of Unit 3. If gypsum/anhydrite saturation occurred just prior to halite saturation, this thick sequence would have to represent a perfectly balanced hydrological steady-state at a

constant degree of evaporation for the entire interval over which Unit 2 was deposited. A much more likely scenario is that gypsum saturation was attained at a sufficiently low degree of evaporation relative to that for halite saturation such that these sulfates precipitated during an interval of decreasing net degree of evaporation in the Onega Basin. More precise interpretations of the relationship between gypsum and halite saturation based on relative thicknesses or volumes of evaporite minerals in the OPH are not possible because important hydrological variables cannot be reconstructed.

The effect of the variables discussed above on f_{Ca} (the fraction of calcium removed prior to halite saturation) and the corresponding $\delta^{44/40}Ca$ range is explored in Fig. S13. The variations in alkalinity, sodium, and chloride are the same as for Fig. S12. The shaded blue regions show permitted seawater chemistry for the OPH, bounded by the appearance of gypsum before halite, the occurrence of magnesium sulfates, and f_{Ca} of at least 0.6. Across the parameter space shown, the lower bound on sulfate concentrations ranges from 7 to 13 mmol/kg. Given the conservative nature of all the boundary conditions, the estimate of 10 mmol/kg presented in the main text is still considered a very probable minimum value, with moderate support for even higher sulfate concentrations.

Comment on calcium concentrations

The oceans have apparently remained undersaturated with respect to gypsum throughout Earth history, given that occurrences of marine gypsum are generally rare and limited to restricted environments. This observation requires an upper bound on the ion activity product for gypsum, defining an additional hyperbolic constraint for seawater composition with respect to the concentrations of calcium vs sulfate. The intersection of this constraint with the linear boundary where magnesium sulfates can be formed under evaporitic conditions yields a maximum possible concentration for calcium at 2.0 Ga (Fig. S14). Further PHREEQC evaporation simulations, performed with other ions as in modern seawater, define this strict maximum to be [Ca] < 40 mmol/kg. Given that sulfate was likely in excess of calcium by some margin (see above), seawater probably lay well below this limit during deposition of the Tulomozero Formation. The maximum calcium concentration defined here is lower than much of the solution space from a recent modeled reconstruction of seawater chemistry and pH (*78*). Compared to those modeled predictions, lower calcium concentrations require higher carbonate ion concentrations and pH as well as lower pCO_2 in order to maintain carbonate saturation.

Comment on Paleoproterozoic sulfur cycle

The large reservoir of marine sulfate at ~2.0 Ga is assumed to have derived primarily from oxidative weathering of pyrite, which corresponds to a seven-electron transfer for sulfur. The scale of the OPH sulfate deposits essentially rules out other potential sources which represent smaller contributions to the global sulfur input flux (e.g. volcanic, hydrothermal). While recycled evaporites may have contributed to the deposition of the OPH salts, the origins and redox implications of those hypothetical precursor evaporites require the same considerations as the OPH evaporites and do not affect the conclusions of this study, apart from implying a slightly older age for the following redox constraints. A concentration of 10 mmol/kg sulfate in a modern-sized ocean represents an oxidative transfer of $\sim 1 \times 10^{20}$ electrons – a massive redox shift to be

accomplished in maximally ~300 million years (from the disappearance of large $\Delta^{33}S$ values to the deposition of the Tulomozero Formation). If all the oxygen produced from the modern organic carbon burial flux (~5×10^{12} mol/yr organic carbon, a four-electron transfer) reacted solely with pyrite, this redox shift would still require 5 million years. Considering other oxygen sinks (notably iron) and the need to maintain a balance of carbon and alkalinity (*26*), accumulating such a large sulfate reservoir over only a few hundred million years is a remarkably rapid transformation. The relationship between the reservoirs of atmospheric oxygen and marine sulfate is not yet clear, beyond the requirement that sufficient oxygen be available to weather pyrite, but the coupling between the sizes of the two reservoirs is probably far from linear.

The sulfur isotopic composition of sulfate minerals presented in this study agrees with previous work on the OPH evaporites (*30*). However, the majority of these $\delta^{34}S$ values are lower than those measured elsewhere in the Tulomozero Formation from trace sulfate relicts and carbonate-associated sulfate (*22*) as well as in carbonate deposits of roughly similar age (*28*). In the OPH core, the uppermost sample in Unit 2 records a higher $\delta^{34}S$ value (9.5‰) than all other samples from lower in Units 1 and 2, leading to the possibility that the seawater sulfur isotopic composition was rising during deposition of the Tulomozero Formation and that the $\delta^{34}S$ analyses from other cores where the Tulomozero Formation was sampled correlate with Unit 3 of the OPH and are also accurate.

The relatively low sulfate $\delta^{34}S$ values measured in the OPH carry implications for the Paleoproterozoic sulfur cycle. The isotopic composition of the sulfur weathering input was likely close to 0‰ throughout the Archean (*79*) and similar in the Paleoproterozoic. The sulfur isotopic composition of seawater sulfate is expected to evolve to higher values as the seawater sulfate reservoir increases and fractional burial of pyrite preferentially sequesters ^{32}S into sedimentary systems. The OPH data suggest that the seawater sulfate reservoir was large at the time of deposition, yet the sulfur isotopic composition of this reservoir was still only slightly above the hypothesized input value of 0‰. It is possible to maintain low seawater sulfate $\delta^{34}S$ values if pyrite burial is not widespread (which is unlikely) or the sulfur isotopic composition of pyrite that is buried has isotopically higher ratios (less ^{32}S). One potential mechanism for burying pyrite during this interval with higher $\delta^{34}S$ values is by converting a larger fraction of the sulfide produced during microbial sulfate reduction to pyrite in semi-closed system conditions, such that the isotopic composition of the pyrite approaches that of seawater sulfate.

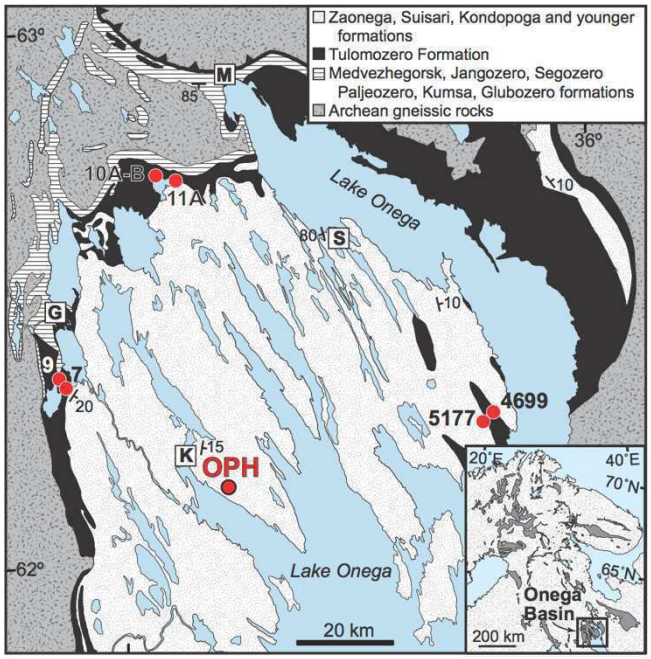

Fig. S1.

Simplified geology of the Onega Basin. Circles show locations of the Onega Parametric Hole (OPH), FAR-DEEP holes 10A-B and 11A, and Onega holes 7, 9, 4699, and 5177. Squares show towns: G–Girvas, K–Kondopoga, M–Medvezhegorsk, S–Shunga. Inset map shows location of Onega Basin and Paleoproterozoic outcrops (darker gray) across the eastern Fennoscandian Shield.

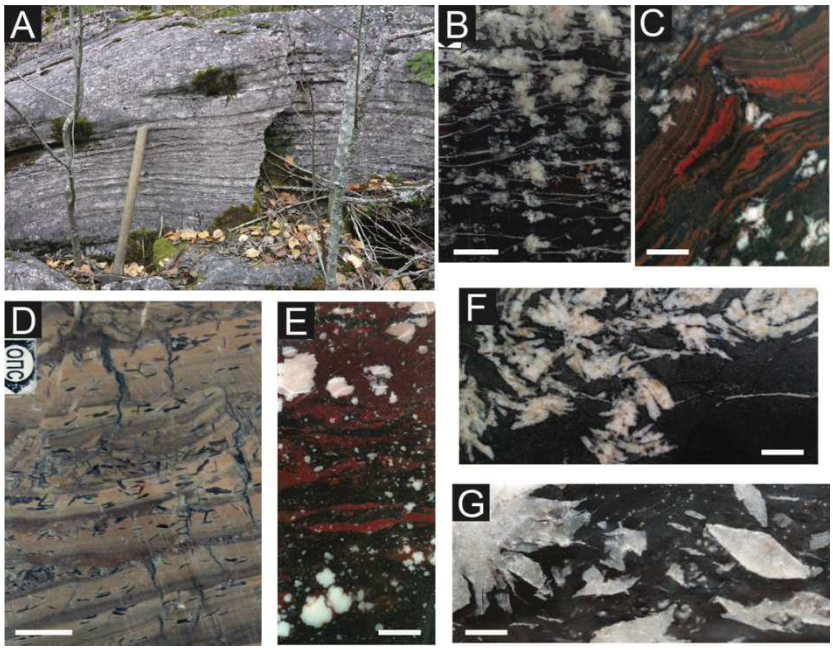

Fig. S2.

Representative Tulomozero Formation evaporite rocks in the OPH and related cores (see Fig. S1 for locations). **A.** Large stromatolite in outcrop near Girvas (hammer for scale). **B.** Chicken-wire fabric in laminated mudstone (2298 m depth OPH core). **C.** Tepee structure in laminated mudstone with calcium-sulfate pseudomorphs (667 m depth core 4699). **D.** Swallow-tail gypsum pseudomorphs in mudstone (2301 m depth OPH core). **E.** Nodular calcium-sulfate pseudomorphs in red-gray mudstone (2228 m depth OPH core). **F.** Bladed calcium-sulfate pseudomorphs in brown-gray mudstone (156 m depth core 9). **G.** Lath and rosette calcium-sulfate pseudomorphs (74 m depth FAR-DEEP core 10A). White bars are 1 cm in length.

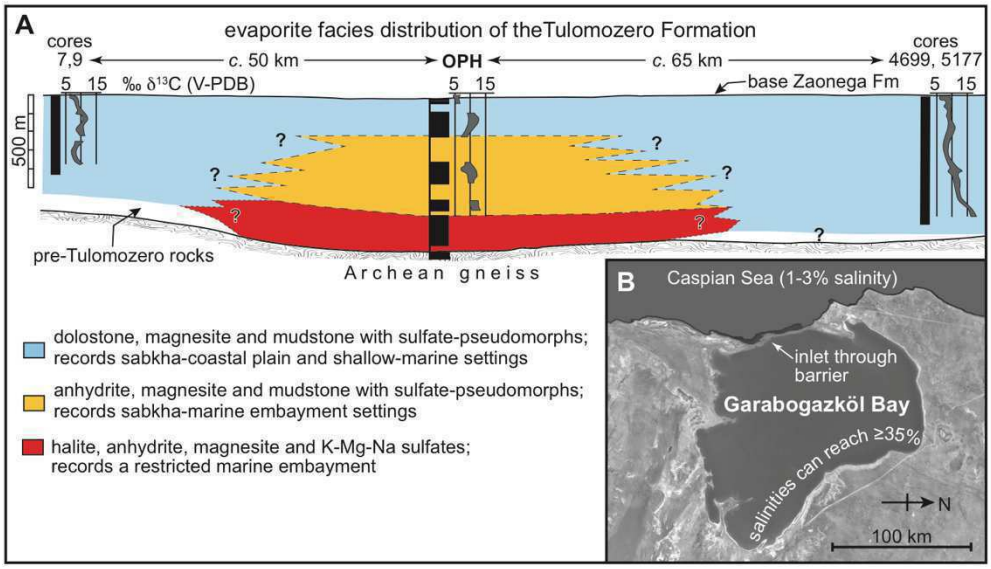

Fig. S3.

A. Basinal stratigraphic framework and carbonate carbon isotope trends of the Tulomozero Formation. Data for the OPH are from (*17*) and for cores 7, 9, 4699, and 5177 from (*18*) (see Fig. S1 for locations). **B.** Garabogazköl Bay, Turkmenistan (satellite image from Google Earth).

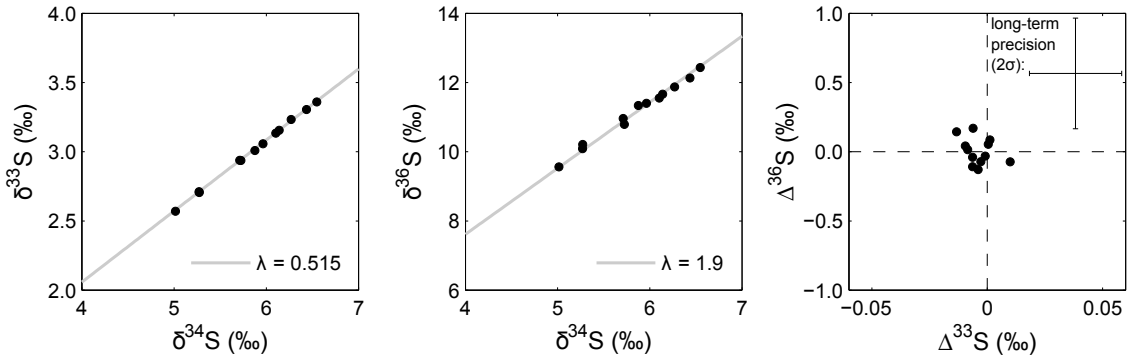

Fig. S4.

Triple-isotope and Δ-Δ plots for multiple sulfur isotope analyses.

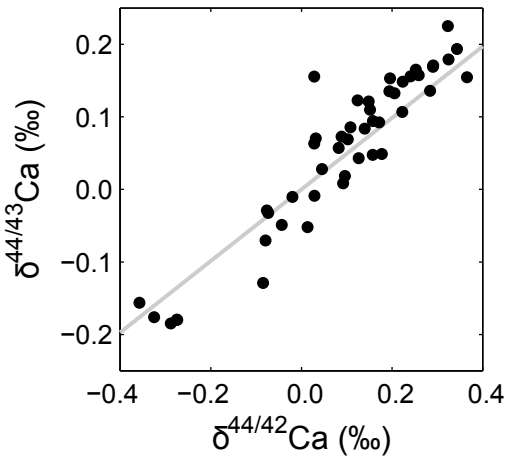

Fig. S5.
Triple-isotope plot for raw calcium isotope data (not normalized to seawater).

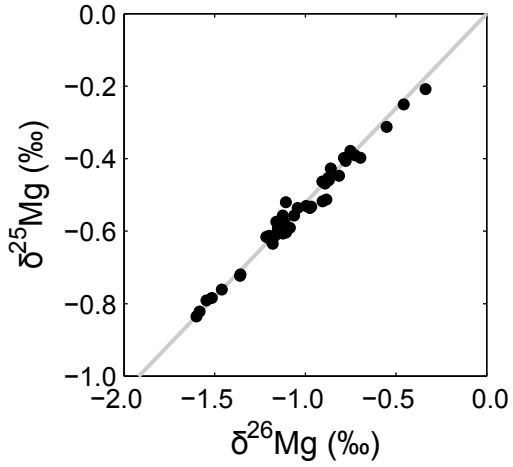

Fig. S6.
Triple-isotope plot for magnesium isotope data.

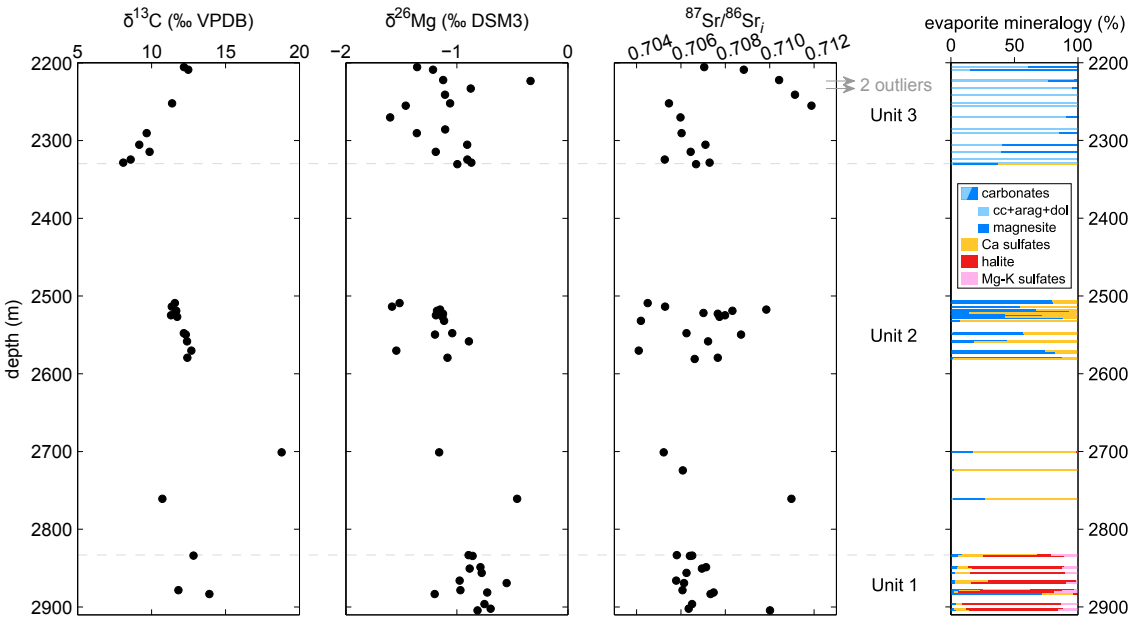

Fig. S7.

Carbon, magnesium, and strontium isotope data, with evaporite mineralogy reproduced from Fig. 2. Strontium isotope ratios have been corrected for formation age.

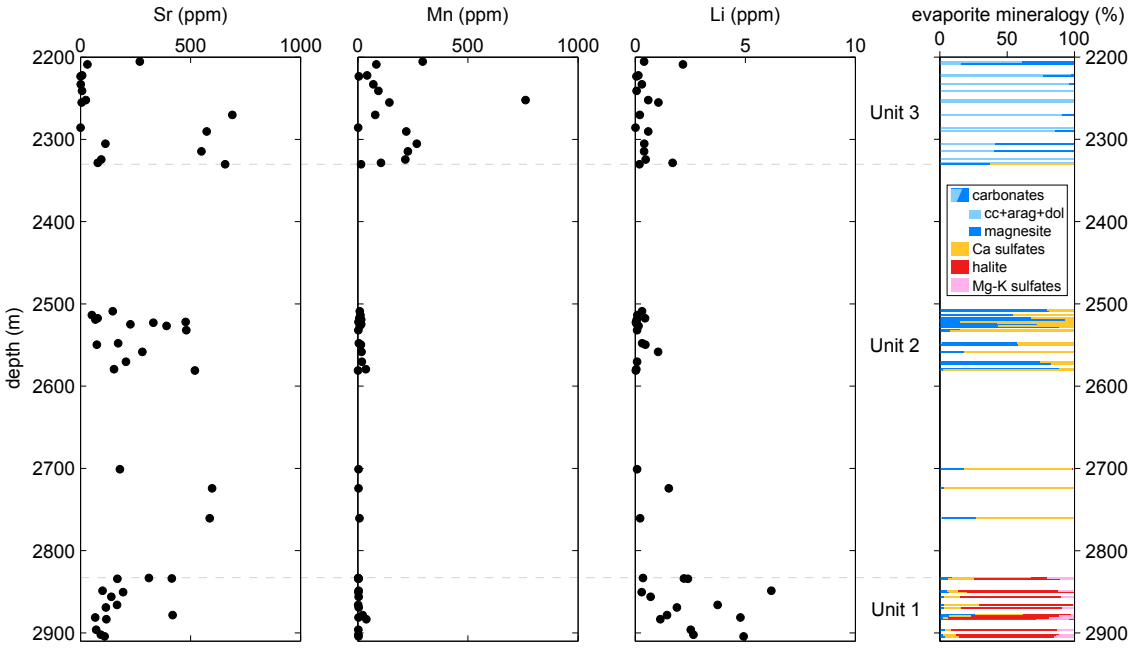

Fig. S8.

Trace element concentrations for the acetic-acid-soluble evaporite minerals, with evaporite mineralogy reproduced from Fig. 2.

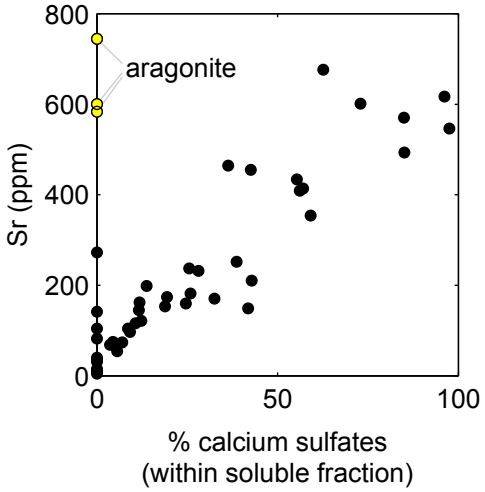

Fig. S9.

Relationship between strontium and calcium sulfate content, indicating the influence of precursor aragonite on three samples (now predominantly composed of other carbonate minerals).

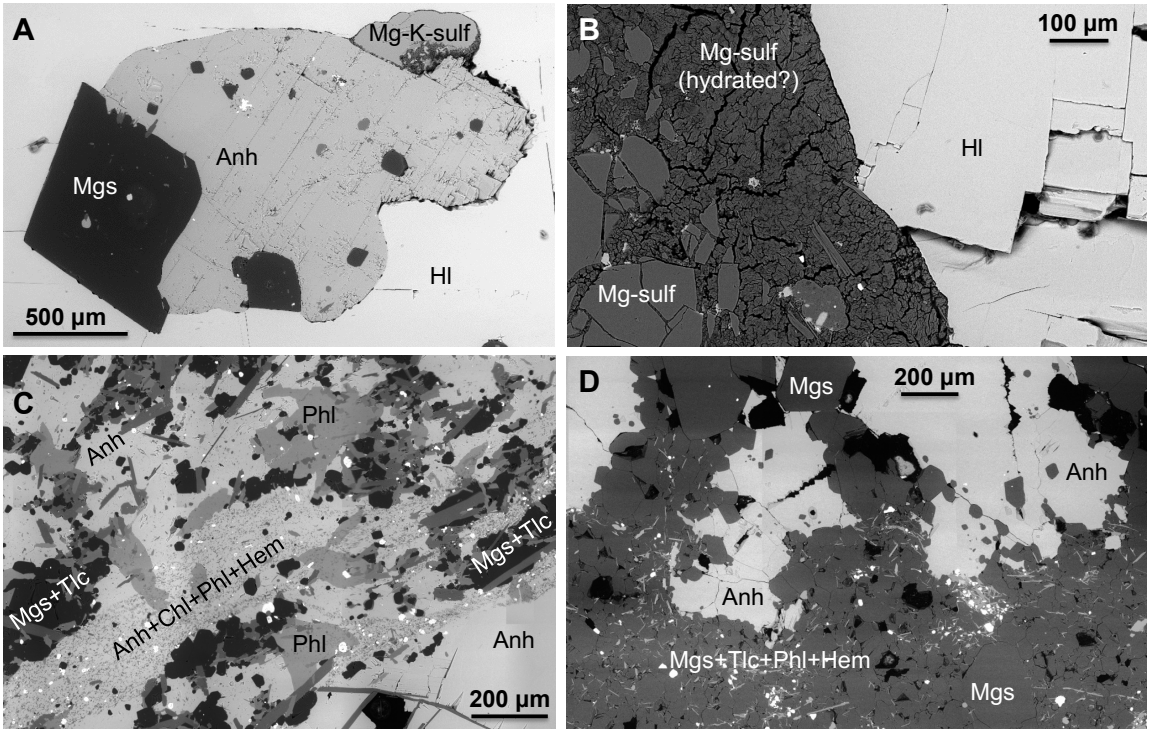

Fig. S10.

Scanning electron microscopy backscattered electron (SEM-BSE) images illustrating characteristic petrographic fabrics of evaporites in the OPH core. **A.** Intraclast of magnesite-anhydrite within halite (Unit 1, 2902 m depth). Note magnesite inclusions within anhydrite and magnesium-potassium-sulfate phase attached to anhydrite. **B.** Magnesium sulfates in halite (Unit 1, 2849 m depth). The two magnesium-sulfate phases have similar EDS spectra but different backscatter intensities, possibly from increased structural water in the darker phase (lower BSE intensity) that appears to be replacing the brighter magnesium-sulfate phase. **C.** Rare preservation of early generation, finely crystalline anhydrite containing inclusions of chlorite, phlogopite and hematite (tilted layer in the middle of image), in contrast to larger recrystallized anhydrite crystals (lower right) without inclusions (Unit 2, 2700 m depth). Magnesite in the inclusion-rich ('muddier') intervals is typically intergrown with and crosscut by secondary talc and phlogopite crystals. **D.** Typical recrystallized magnesite-anhydrite fabric (upper part of image) with large, inclusion-free crystals; early generation, finer-grained magnesite (lower part of image) occasionally preserved in association with dispersed talc, phlogopite and hematite (Unit 2, 2521 m depth).

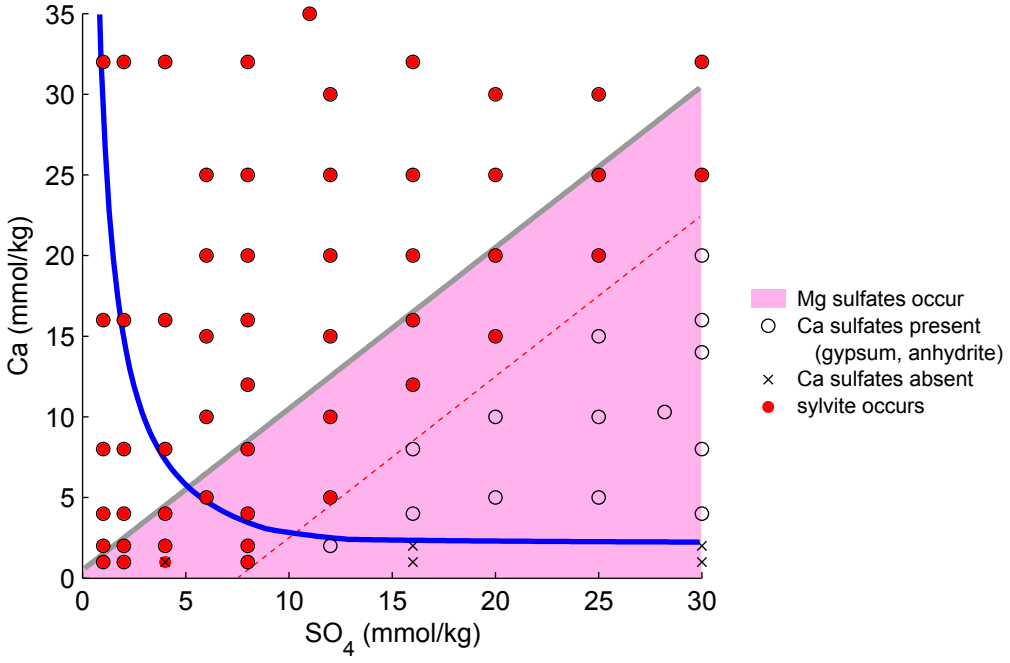

Fig. S11.

Mineral assemblages from simulated batch evaporation of seawater with variable calcium and sulfate concentrations (all other ions equal to modern seawater). Blue line indicates the boundary for the appearance of gypsum before halite (same as Fig. 3 in main text).

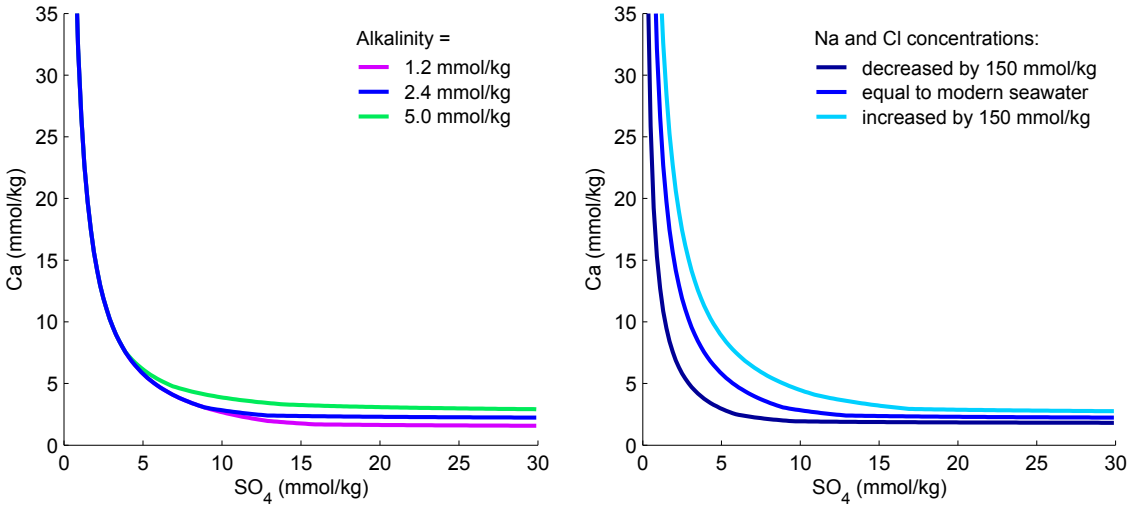

Fig. S12.

Effect of different concentrations of alkalinity (left) and sodium and chloride (right), relative to modern seawater (middle blue lines), on the appearance of gypsum before halite in batch evaporation simulations. Much greater alkalinity is not permitted, as calcium concentrations would be correspondingly lower and gypsum would not precipitate in the observed evaporite sequence.

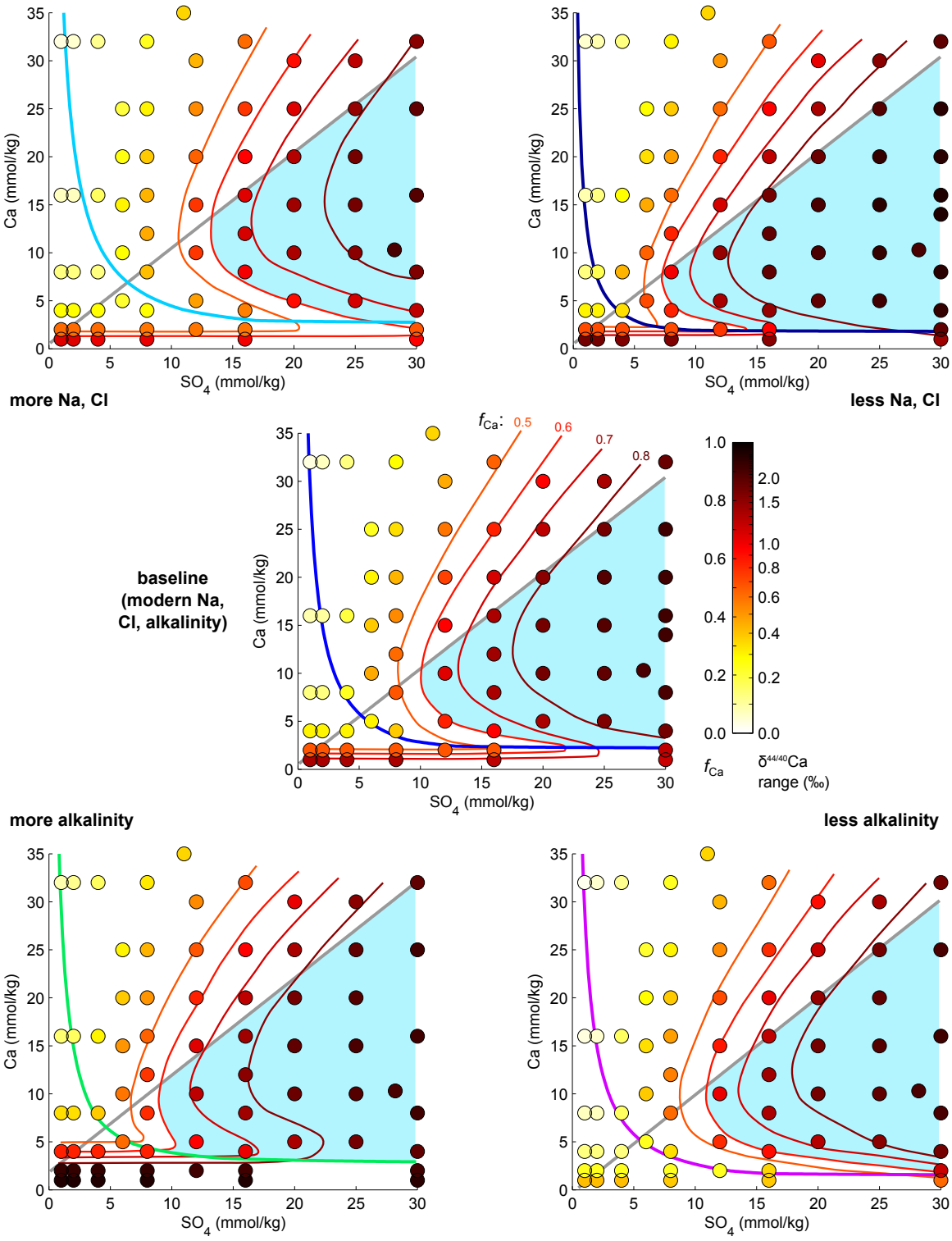

Fig. S13.

Effect of different concentrations of alkalinity (bottom) and sodium and chloride (top) on the evaporitic distillation of calcium (changes in concentration the same as for Fig. S12) and other mineralogical boundaries. Central plot shows baseline behavior, with boundary lines and blue shaded region the same as in Fig. 3 (main text).

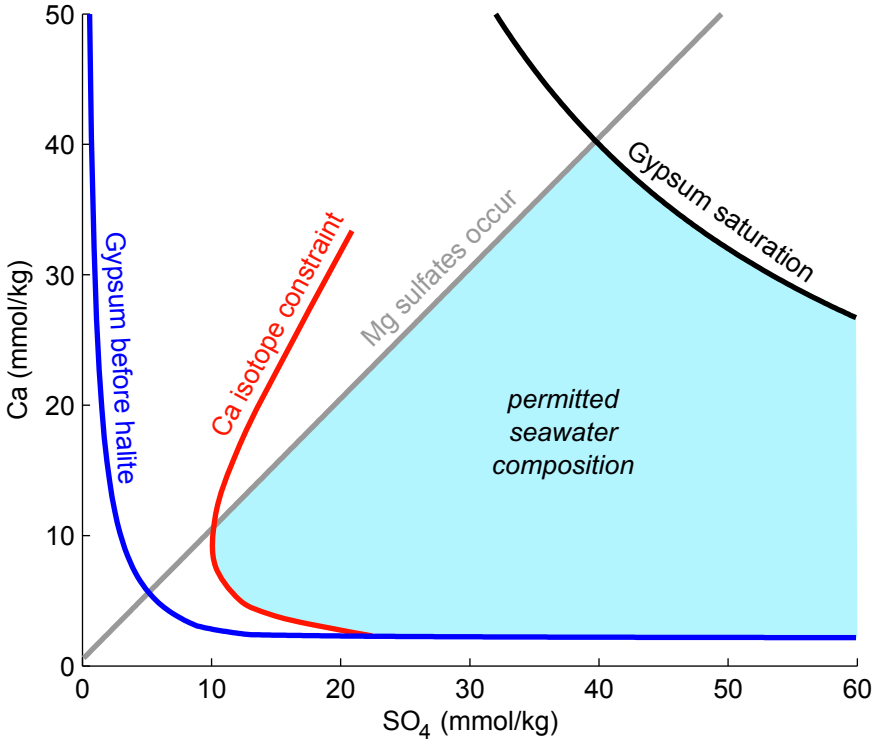

Fig. S14.

An expanded view of the seawater chemistry constraints from the OPH evaporites (Fig. 3 in main text), including the boundary for gypsum saturation (black line). Calcium concentrations between ~2.5 and 40 mmol/kg are permitted, with this range establishing additional constraints (not shown) for carbonate ion concentration and aqueous carbonate chemistry.

Table S1.

Evaporite minerals included in the PHREEQC equilibrium assemblage, with thermodynamics specified in pitzer.dat.

Mineral	Formula
anhydrite	$CaSO_4$
bischofite	$MgCl_2 \cdot 6\ H_2O$
bloedite	$Na_2Mg(SO_4)_2 \cdot 4\ H_2O$
calcite	$CaCO_3$
carnallite	$KMgCl_3 \cdot 6\ H_2O$
celestine	$SrSO_4$
epsomite	$MgSO_4 \cdot 7\ H_2O$
glauberite	$Na_2Ca(SO_4)_2$
gypsum	$CaSO_4 \cdot 2\ H_2O$
halite	NaCl
hexahydrate	$MgSO_4 \cdot 6\ H_2O$
kainite	$KMgClSO_4 \cdot 3\ H_2O$
kieserite	$MgSO_4 \cdot H_2O$
leonhardite*	$MgSO_4 \cdot 4\ H_2O$
leonite	$K_2Mg(SO_4)_2 \cdot 4\ H_2O$
$MgCl_2$ dihydrate	$MgCl_2 \cdot 2\ H_2O$
$MgCl_2$ tetrahydrate	$MgCl_2 \cdot 4\ H_2O$
mirabilite	$Na_2SO_4 \cdot 10\ H_2O$
pentahydrate	$MgSO_4 \cdot 5\ H_2O$
polyhalite	$K_2MgCa_2(SO_4)_4 \cdot 2\ H_2O$
schoenite**	$K_2Mg(SO_4)_2 \cdot 6\ H_2O$
sylvite	KCl
thenardite	Na_2SO_4

*Leonhardite reflects usage in PHREEQC, but denotes leonhardtite, also known as starkeyite. **Schoenite also known as picromerite.

Data table S1 (separate file).
Mineralogical composition of sediments in the OPH core (from XRD analysis).

Data table S2 (separate file).
Geochemical data from OPH samples.